Improvements of a process-based model for 2- and 3-dimensional simulation of flow in presence of various obstructions

Florian GANTHY[1,*], Romaric VERNEY[2], Franck DUMAS[3,4]

[1] Ifremer, LITTORAL, F-33120 Arcachon, France

[2] Ifremer, DYNECO, DHYSED, F-29280 Plouzané, France

[3] SHOM, Physical research department, F-29238 Brest, France

[4] University Brest, CNRS, Ifremer, LOPS, IUEM, F-29280 Plouzané, France

* ***Corresponding author***: Florian GANTHY, florian.ganthy@ifremer.fr, Telephone: +33(0)5 57 72 29 98

Abstract

In coastal areas, various types of biological and anthropic structures significantly influence the flow and related sediment dynamics. In this paper we have developed a generic flow-obstruction module, designed to represent both upward or downward, rigid or flexible structures, using a limited number of parameters. This module can be integrated to any hydrodynamic coastal model. The obstruction/flow interactions module can operate either in 3D or 2D mode. It calculates source terms used in momentum equation and in the k-ε turbulent closure model (exclusive to 3D mode). Additionally, the module allows for the incorporation of multiple obstructions within a single mesh, which is invaluable when modelling realistic ecosystem dynamics. The module's validation was carried out using flume experiments on seagrasses, as well as using numerical studies involving two anthropogenic structures: mussel long-lines and oyster tables. The coupled hydrodynamic/obstruction model yielded excellent results for 2D/3D velocity fields with minimal calibration efforts. This module offers the potential to explore the future trajectories of vulnerable coastal systems in response to global change, or to identify restoration measures in engineered coastal systems.

Keywords: Obstructed flow, Submarine vegetation, Anthropic structures, Turbulence, Hydrodynamic modelling

1. Introduction

In coastal areas, various types of biological and anthropic structures are prevalent, including seagrass beds, salt-marshes vegetation, oyster tables, mussel posts, rafts, and lines, among others. These structures interact significantly with hydrodynamics. They are directly influenced by the flow, and in turn, they locally and regionally modify (seagrass beds: Fonseca and Fisher, 1986; Nepf, 1999; salt-marshes vegetation: Bouma *et al.*, 2007; oyster tables: Kervella *et al.*, 2010; mussel posts: Delaux *et al.*, 2011). By damping hydrodynamic energy from tidal currents and waves, these obstructions strongly influence the transport of dissolved and particulate substances, such as sediments, nutrients, pollutants and larvae. Directly or indirectly, they also modulate erosion-deposition processes, thereby impacting the morphological evolution of coastal ecosystems across various spatial and temporal scales (Temmerman *et al.*, 2005; Le Hir *et al.*, 2007; Fagherazzi *et al.*, 2012).

More specifically, seagrasses are often referred to as ecosystem engineers because they locally attenuate currents and waves, promoting sediment deposition and retention (Ward *et al.*, 1984; Lacy and Wyllie-Echeverria, 2011; Ganthy *et al.*, 2015). Increased water clarity resulting from this sediment trapping enhances light penetration, fostering their photosynthetic activity and potential growth (Carr *et al.*, 2010). Oyster and mussels farming techniques lead to sediment accumulation beneath and around the structures (Sornin, 1981), attributable to both reduced flow energy and bio-deposition (Kaiser *et al.*, 1998). This induces cascading effects on nutrient fluxes, benthic fauna and shellfish production itself (Harstein *et al.*, 2004; Giles *et al.*, 2006; Weise *et al.*, 2009).

In the context of global change, evaluating and predicting changes in the status of coastal habitats and ecosystems has become increasingly important for coastal managers and scientists (Montefalcone, 2009). Considering the effects of various obstructions on hydrodynamics and, subsequently, on the transport of dissolved and particulate matter is critical for estimating the ecological and morphological status and trajectories of coastal ecosystems. However, due to the inherent complexity of coastal ecosystems (*e.g.*, complex morphology, spatio-temporal variations in vegetation distribution and/or shellfish farming structures, non-linearity between hydro-sedimentary processes), laboratory or field data cannot be directly extrapolated to a large coastal scale. Coastal numerical models offer powerful complementary capabilities to investigate these complex processes and the potential ecosystem response to future changes in environmental forcing or human pressures.

Over the past few decades, several studies have simulated the effects of various benthic vegetation (*i.e.*, flexible/rigid, submerged/emerged) on flow (*e.g.*, Morin *et al.*, 2000; Abdelrhman, 2003; Temmerman *et al.*, 2005; Gao *et al.*, 2011; Zhang *et al.*, 2013; Kombiadou *et al.*, 2014; Weitzman *et al.*, 2015; Beudin *et al.*, 2017). However, most of these studies were either species-specific or dedicated to small-scale investigations without being applied at the scale of an entire coastal system. Only a few coastal models account for the three-dimensional effects of benthic vegetation on mean and turbulent flows (Temmerman *et al.*, 2005; Kombiadou *et al.*, 2014; Beudin *et al.*, 2017; Donatelli *et al.*, 2018). Even fewer studies have addressed the simulation of hydrodynamics in the presence of shellfish farming structures (Delaux *et al.*, 2011; Gaurier *et al.*, 2011; Duarte *et al.*, 2014), with similar limitations observed in vegetation-flow modelling (*i.e.*, only a few models dedicated to the scale of a coastal system). Furthermore, no coastal model is currently capable of simulating the three-dimensional cumulative effects of complex associations of flow obstructions (*e.g.*, seagrass beds located beneath oyster tables or mussel lines, multi-specific assemblages of benthic vegetation) on water flow.

Within this context, the present work focuses on the comprehensive description of recent improvements made to a generic flow-obstruction module previously described by Kombiadou *et al.* (2014) for the specific case of the seagrass *Zostera noltei* and applied to the Arcachon Bay. These module improvements include: (1) the development of a generic module adapted to various types of natural and anthropogenic obstructions found in coastal ecosystems (i.e., rigid/flexible, submerged/emerged, upward/downward); (2) the ability to define multiple obstruction types within the same grid cell; and (3) the utilization of a minimal, optimized number of empirical calibration parameters. The present paper encompasses small-scale module validation, sensitivity analysis, and a discussion on potential module limitations and future improvements.

2. Methods

The flow-obstruction module, referred to as the OBSTRUCTIONS module, was initially implemented within the MARS model (Model for Application at Regional Scale; Lazure and Dumas, 2008). The MARS model is a three-dimensional, primitive equations, split implicit free surface, sigma coordinate hydrodynamic model designed to simulate flows across various coastal areas, ranging from regional scales (i.e., continental shelves) to local scales (i.e., small bays and estuaries). The OBSTRUCTIONS module has been designed for easy coupling with any hydrodynamic model that shares similar specifications and is currently being integrated into the CROCO model (https://croco-ocean.org/).

The MARS model couples barotropic and baroclinic modes and solves the primitive equations (Navier-Stokes equations based on the classic Boussinesq and hydrostatic hypotheses) using a semi-implicit scheme with finite differences on an Arakawa C grid. Bottom friction is computed based on the approximation of constant turbulent stress between the first computed velocity level and the bottom, leading to a user-defined roughness length (z_0). Additionally, the vertical turbulence closure scheme is formulated in a unified manner (Generic Length Scale) according to Umlauf and Burchard (2003), encompassing *k-kl*, *k-ε*, or *k-ω* formulations.

To prevent the creation of very thin sigma layers at low water depths, the baroclinic mode is terminated below a user-defined water level threshold value. In such cases, advection is performed as depth-averaged, and vertical velocity profiles are theoretically computed based on the classical Law of the Wall method.

The MARS modelling platform (https://mars3d.ifremer.fr; in French) also includes additional modules that allow for the coupling of hydrodynamics, sediment dynamics, biogeochemical cycles, and ecological models for phytoplankton and seagrass growth (see, among others, Guillaud *et al.*, 2000; Plus *et al.*, 2003; Le Hir *et al.*, 2011; Huret *et al.*, 2013; Mengual *et al.*, 2017). The present work represents a significant advancement in the development of an integrated, fully coupled ecosystem model, bridging the gap between physics, ecology, and human impacts.

2.1. Description of the OBSTRUCTIONS module

The OBSTRUCTIONS module has been integrated with the hydrodynamic MARS model. Initially designed to characterize the three-dimensional hydrodynamic effects of flexible seagrass *Zostera noltei* on flow (Kombiadou *et al.*, 2014), the module has been updated to allow the simulation of various types of obstructions (Figure 1). The numerical scheme has also been modified to accommodate multiple obstructions within the same grid cell (*e.g.*, seagrass and oyster tables), and the computation procedure for the height of flexible obstructions has been refined. Additionally, a theoretical velocity profile has been introduced for cases where baroclinic computation is terminated due to shallow water depths. This enhancement aims to better replicate bottom velocities used to compute bottom shear stress when simulating sediment dynamics. These new developments are detailed below.

Currently, the module can account for three generic types of obstructions (Figure 1a):

- ***Upward obstructions*** (**UP**): Obstructions that start from the seabed and extend upwards towards the water surface (*e.g.*, vegetation, mussel posts). These obstructions can be either rigid or flexible.
- ***Downward obstructions*** (**DO**): Obstructions that start from the water surface and hang downwards towards the seabed (*e.g.*, mussel/oyster lines). Similar to UP types, these obstructions can be either rigid or flexible.
- ***Three-dimensional obstructions*** (**O3D**): A specific subtype of the upward type, O3D describes obstructions located in mid-water, without structures near the seabed or surface. This particular type is typically used to represent oyster bags and is associated with an UP obstruction to simulate oyster tables.

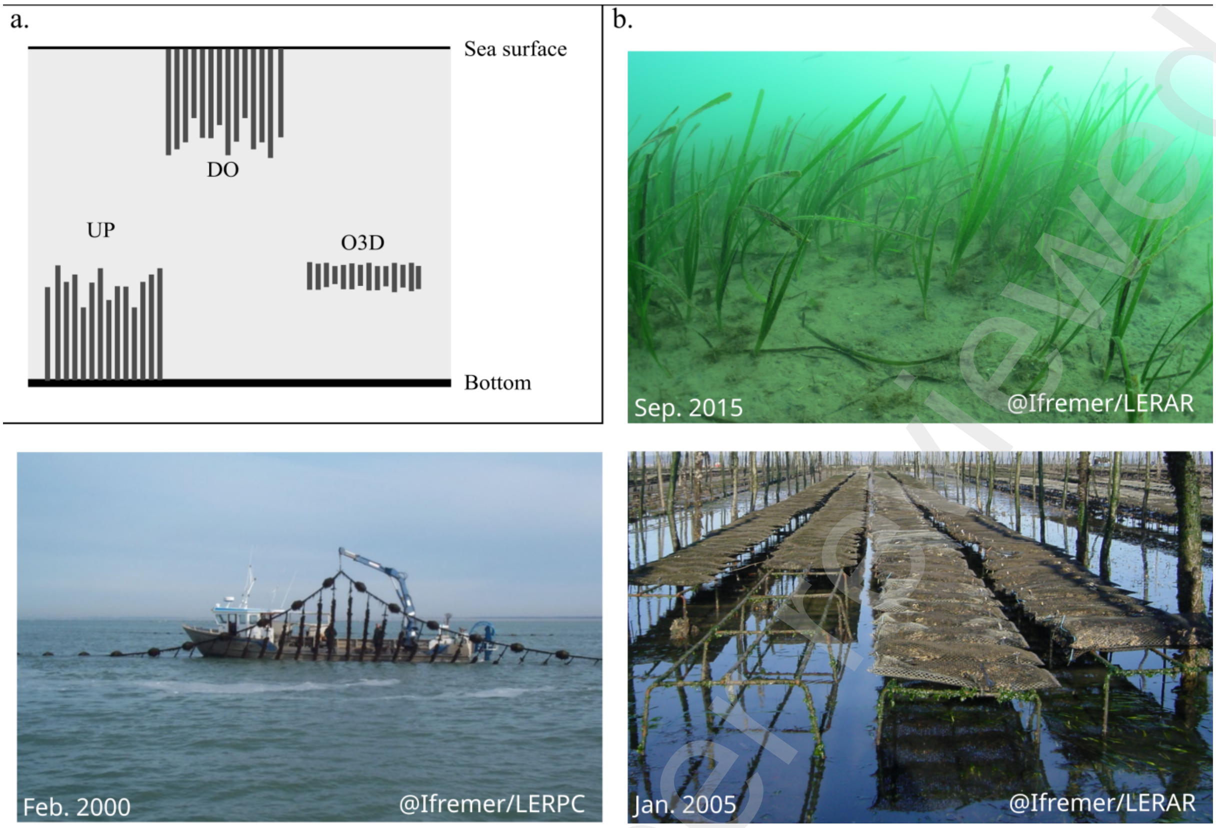

Figure 1: (a.) simplified representation of the three types of obstructions allowed within the module and (b.) pictures of real obstructions to be simulated: seagrass meadows (upper right), mussel long-line (lower left) and oyster tables (lower right).

2.1.1. 3D equations for obstruction/flow interactions

The influence of obstruction elements on three-dimensional flow is accounted for by: i) the loss of momentum due to the drag exerted on obstruction elements, and ii) the balance between turbulence production and dissipation introduced within the *k-ε* turbulence closure scheme. This scheme is primarily used in coastal environments (Temmerman *et al.*, 2005; Casamitjana *et al.*, 2012) and is one of the simplest models suitable for flow-obstruction modeling (Uittenbogaard, 2003).

Each obstruction element can be described in two ways depending on its geometry: cylinder-like (*e.g.*, reeds or mussel ropes, Figure 2a) or parallelepiped-like (*e.g.*, seagrass leaves, Figure 2b). For the cylinder-like case, obstructions are characterized by their diameter ($d_0(z)$, m) and the number of elements per unit area ($n(z)$, m^{-2}), referred to as element density hereafter. In the parallelepiped-like case, the diameter is replaced by the obstruction's width ($w(z)$, m) and thickness ($t_0(z)$, m), where z refers to the height above the bed, corresponding to the vertical mesh grid of the hydrodynamic model.

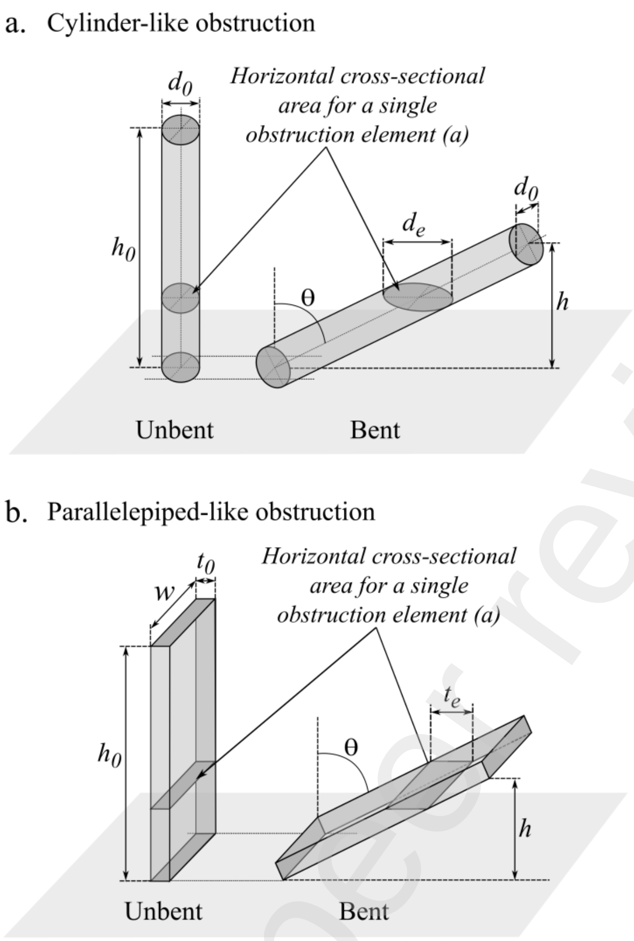

Figure 2: Schematic representation of a single obstruction element, (a.) for cylinder-like element, and (b.) for parallelepiped-like element. For bent case, variables are described in section 2.1.3.

The drag induced by all obstruction elements is accounted for as a momentum loss term (friction force) in *x* and *y* directions:

$$F_u(z) = -\cdot\frac{1}{2}\cdot C_D\cdot\rho\cdot d_0(z)\cdot n(z)\cdot u(z)\cdot\sqrt{u(z)^2+v(z)^2}\cdot f_z(z)\cdot f_{xy}(z) \tag{1a}$$

$$F_v(z) = -\cdot\frac{1}{2}\cdot C_D\cdot\rho\cdot d_0(z)\cdot n(z)\cdot v(z)\cdot\sqrt{u(z)^2+v(z)^2}\cdot f_z(z)\cdot f_{xy}(z) \tag{1b}$$

In the equations above, corresponding to the cylinder-like case, C_D is the drag coefficient for obstructions (-), ρ is the water density (kg.m^{-3}), $u(z)$ and $v(z)$ are the horizontal flow velocities (m.s^{-1}) in x and y directions, respectively, $f_z(z)$ and $f_{xy}(z)$ represent the vertical fraction of the layer and the horizontal fraction of the grid cell effectively occupied by obstructions (-). For the parallelepiped-like case, primarily used to represent seagrass leaves, $d_0(z)$ is substituted by $w(z)$ in equations (eq. 1a and 1b). Indeed, leaf inertia is considered to be weaker in the direction perpendicular to its width, so that leaves are assumed to align with their width facing the flow.

The influence of obstructions on turbulence leads to additional source terms in the equations of the k-ε turbulence closure scheme (Temmerman *et al.,* 2005). The equations for turbulent kinetic energy (k, m^2.s^{-2}, eq. 2) and the turbulent energy dissipation (ε, m^2.s^{-3}, eq. 3) become:

$$\left(\frac{\partial k}{\partial t}\right)_{obstruction} = \frac{1}{1-A(z)} \cdot \frac{\partial}{\partial z}\left\{(1-A(z)) \cdot \frac{\nu+\nu_t}{\sigma_k} \cdot \frac{\partial k}{\partial z}\right\} + T(z) \qquad (2)$$

$$\left(\frac{\partial \varepsilon}{\partial t}\right)_{obstruction} = \frac{1}{1-A(z)} \cdot \frac{\partial}{\partial z}\left\{(1-A(z)) \cdot \frac{\nu+\nu_t}{\sigma_\varepsilon} \cdot \frac{\partial \varepsilon}{\partial z}\right\} + T(z) \cdot \tau_\varepsilon^{-1} \qquad (3)$$

Where $A(z)$ is the horizontal cross-sectional obstruction area per unit area (-) at level z (eq. 4a for cylinder-like case and eq. 4b for parallelepiped-like case respectively), ν and ν_t are molecular and eddy viscosities (m^2.s^{-1}), σ_k and σ_ε are turbulent Prandtl-Schmidt numbers for self-mixing turbulence (σ_k=1 and σ_ε=1.3). $T(z)$ represents the work spent by the fluid (m^2.s^{-3}) at level z (eq. 5) and τ_ε is the energy dissipation timescale (eq. 6), which corresponds to the minimum value between the dissipation of free turbulence and the dissipation of eddies between obstruction elements.

$$A(z) = \frac{\pi}{4} \cdot d_0(z)^2 \cdot n(z) \cdot f_{xy}(z) \qquad (4a)$$

$$A(z) = w(z) \cdot t_0(z) \cdot n(z) \cdot f_{xy}(z) \quad (4b)$$

$$T(z) = \frac{\sqrt{\left(F_u(z) \cdot u(z)\right)^2 + \left(F_v(z) \cdot v(z)\right)^2}}{\rho} \quad (5)$$

$$\tau_\varepsilon = MIN\left[\frac{1}{c_{2\varepsilon}} \cdot \left(\frac{k}{\varepsilon}\right), \frac{1}{c_{2\varepsilon} \cdot \sqrt{c_\mu}} \cdot \left(\frac{L(z)^2}{T(z)}\right)^{1/3}\right] \quad (6)$$

$$L(z) = c_{lz} \cdot \sqrt{\frac{1 - A(z)}{n(z)}} \quad (7)$$

The values of coefficients $c_{2\varepsilon}$ and c_μ are 1.96 and 0.09, respectively (Temmerman *et al.*, 2005). *L(z)* represents the typical size of eddies, which is limited by the smallest distance between obstruction elements. For rigid vertical cylinders, c_{lz}≈1.0, whereas lower values (c_{lz}≈0.3) have been found to be applicable for flexible vegetation (Uittenbogaard, 2003).

2.1.2. 2D equations for obstruction/flow interactions

In the barotropic mode, the friction terms ($F_u(z)$ and $F_v(z)$) are depth-averaged and introduced within the barotropic momentum equation. Additionally, for near-bed velocity analysis and sediment dynamics (i.e., computation of bottom shear stress), a theoretical computation of the velocity profile is conducted when the baroclinic mode is terminated. Currently, this is computed only for upward obstructions (UP).

When obstructions occupy more than 90% of the total water depth, they are considered as emergent or nearly emergent. In such cases, velocity profiles are computed using the user-defined roughness length (z_0, m), in accordance with the classical Law of the Wall method. For emergent obstructions the bottom boundary layer is likely to develop near the bed, while no shear layer exists at the top of obstructions (Nepf and Vivoni, 2000). The decision not to differentiate between emergent (100% of water depth occupied by obstructions) and nearly-emergent (occupying 90% to 100% of water depth) was made to avoid spurious (excessively high) velocities above obstructions, which could lead to numerical instabilities.

Note that the roughness-length (z_0) is defined as the bed roughness length, not the total roughness induced by both the bed and the obstructions. For obstructions occupying less than 90% of the total water-depth (considered fully submerged), velocity profiles are computed using the two-layer method fully described by Abdelrhman (2003) and summarized in Appendix A. The coefficient of proportionality (c) found in equations (5) to (7) in Abdelrhman (2003) will be referred to as $c_{z0,abd}$ later in this paper. This coefficient requires calibration.

2.1.3. Geometrical considerations on obstruction flexibility

In the case of flexible obstructions (*e.g.*, vegetation…), the obstruction elements interact with the ambient current flow while bending. This interaction leads to changes in obstruction height (h), element density ($n(z)$), and horizontal cross-sectional area ($A(z)$), depending on their bending angle ($\theta(z)$). After computing the bent obstruction height and bending angle, $A(z)$ is then calculated, taking into account the geometrical modification of the projected horizontal surface area (Figure 2).

For cylinder-like case, $A(z)$ is considered as an ellipsis, depending on $d_0(z)$, the obstruction diameter and $d_e(z)$, the projected obstruction diameter in the flow direction. Meanwhile for parallelepiped-like case, $A(z)$ is considered as a rectangle, depending on $w(z)$, the obstruction width, and $t_e(z)$, the projected obstruction thickness in the flow direction.

Regarding the calculation of bent height (*h*) and bending angle ($\theta(z)$), the obstruction height in the previous version of the module was empirically parameterized for seagrass *Zostera noltei* from flume data through a polynomial formulation that depended on depth-averaged velocity and the Leaf Area Index (LAI) of the seagrass canopy (Kombiadou *et al.*, 2014). With this polynomial regression, the computed obstruction height had to be bounded to prevent unrealistic (negative) obstruction heights. Following Ganthy *et al.* (2015), the previous polynomial formulation has been replaced by a more robust empirical formulation that corresponds to an exponential decrease in canopy height whith increasing depth-averaged free-stream velocity:

$$h = h_0 \cdot \exp(-c_h \cdot U_\infty) \qquad (8)$$

Where h_0 is the unbent obstruction height, c_h is a calibration coefficient (3.6 for seagrass *Z. noltei*, Ganthy *et al.*, 2015) and U_∞ is the depth-averaged free-stream velocity. Using this empirical parameterization, the bending angle ($\theta(z)$, in radians) is considered constant for all layers occupied by obstructions, such that $\theta(z)=arccos(h/h_0)$.

As a second option, a physically-based formulation has also been implemented. This formulation, fully described in Abdelrhman (2007) and summarized in Appendix B, is based on the balance between drag, lift, friction, weight, and buoyancy forces on a single obstruction element, subdivided into a user-defined number of segments (n_{seg}, Figure 3). This method, which neglects elasticity of obstruction elements, is particularly adapted to highly flexible obstructions like seagrasses. An iterative procedure computes the bending angle for each element until the computed height of the total obstruction converges with the flow velocity. Indeed, the vertical position of the elements above the bottom will change according to their bending angle, leading them to experience different local velocities. Using this procedure, the angle of obstruction segment ($\theta(z)$) is directly computed by the algorithm and the bent height (h) is then geometrically reconstructed.

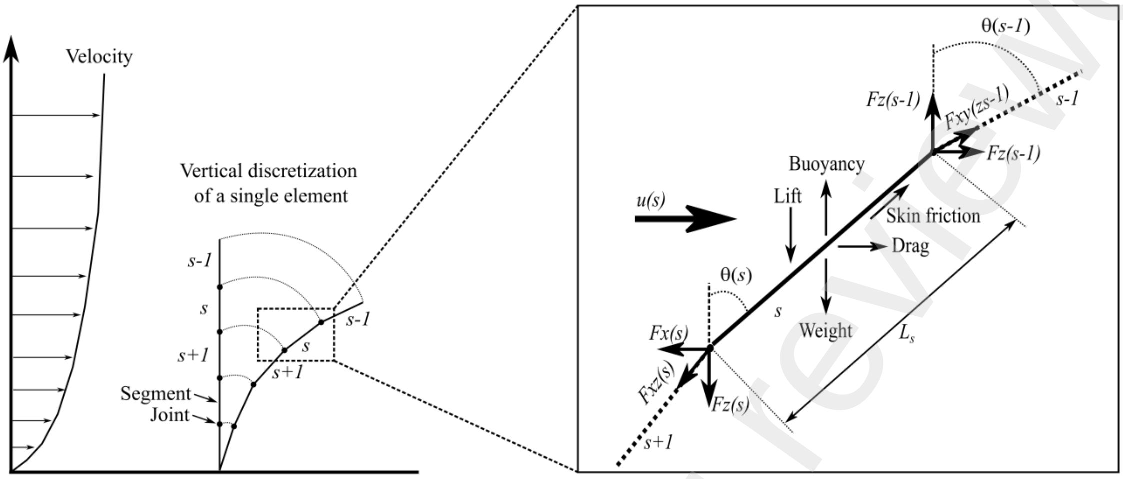

Figure 3: Representation of flexible obstruction element with effects of local current velocity on forces acting on each element segment (adapted from Abdelrhman, 2007).

2.1.4. Multiple obstructions

When multiple types of obstructions are present within a grid cell, the total friction forces ($F_u(z)$ and $F_v(z)$) and the projected horizontal surface area ($A(z)$) are computed as the sum of the friction forces and projected horizontal surface area contributed by each obstruction:

$$F_{u,tot}(z) = \sum_{i=1}^{i=n_{obst}} F_{u,i}(z) \quad (9a)$$

$$F_{v,tot}(z) = \sum_{i=1}^{i=n_{obst}} F_{v,i}(z) \quad (9b)$$

$$A_{tot}(z) = \sum_{i=1}^{i=n_{obst}} A_i(z) \quad (10)$$

In previous equations, i is the index of each obstruction type and n_{obst} is the total number of obstructions. Furthermore, the typical size of eddies ($L(z)$, eq. 7) is then computed as follows:

$$L_{tot}(z) = \frac{\sum_{i=1}^{i=n_{obst}} f_{xy}(z) \cdot c_{lz,i}}{\sum_{i=1}^{i=n_{obst}} f_{xy}(z)} \cdot \sqrt{\frac{1 - A_{tot}(z)}{\sum_{i=1}^{i=n_{obst}} n(z)}} \quad (11)$$

We decided to average the coefficient c_{lz} over all obstructions occupying the cell, weighted by the horizontal cell fraction occupied by each i^{th} obstruction. Although this approach may be questioned, the sensitivity analysis demonstrated that the model's sensitivity to this coefficient is weak (see section 4.1.).

Finally, for very shallow waters, when the hydrodynamics model operates in 2D mode, the required theoretical velocity profiles are computed similarly to the c_{lz} coefficient. They are averaged from the velocity profiles computed for each obstruction, weighted by the horizontal cell fraction occupied by each obstruction.

2.2. Test case configurations

To test the model's behavior, accuracy, and sensitivity in simulating flow-obstruction interactions, four setups were defined based on previous experimental or modeling studies:

- **ZNcase** (*Zostera noltei* case): (sections 2.2.1. and 3.1.) This setup reproduces the flume experiments conducted by Ganthy *et al.* (2015) for the seagrass *Zostera noltei*. It was used for module calibration.
- **ZMcase** (*Zostera marina* case): (section 2.2.2 and 3.2.) This setup replicates the flume experiments by Lefebvre *et al.* (2010) for the seagrass *Zostera marina*. It was used to validate the module.
- **MLLcase** (Mussel Long-Line case): (section 2.2.3 and 4.2.1) This setup is inspired by the modeling experiments of Delaux *et al.* (2011) concerning suspended shellfish structures. It was used to test the downward functionality.

- **OYcase** (Oyster-farm case): (section 2.2.4 and 4.2.2) This setup is inspired by the modelling experiments of Gaurier *et al.* (2011) for oyster farming structures. This test was used to evaluate both the O3D obstructions functionality and the representation of multiple obstructions within the same grid cell.

2.2.1. *Zostera noltei* case (ZNcase)

This case aims at reproducing flume experiments conducted by Ganthy *et al.* (2015). These experiments were carried out in a recirculating straight flume, examining five contrasting seagrass development stages and four flow regimes (V1 to V4, Table 1). This led to twenty velocity profiles measured 0.45 m downstream from the leading edge of the vegetation patch (profile P3 in Ganthy *et al.*, 2005).

All experimental flume conditions, including the dimension of the flume and vegetated bed, water depth, seagrass characteristics, and flow velocities (as listed in Table 2), were simulated using the two-dimensional vertical (2DV) approximation. The horizontal discretization (dx) was set to 0.05 m, while 40 equidistant sigma layers (dz = 0.005 m) were used for vertical discretization. For all five seagrass characteristics and the four flow regimes, the model was run in both 3D mode and 2D modes (with the theoretical reconstruction of velocity profiles) to test the two different formulations.

In all cases, the canopy height was computed using the Abdelrhman (2007) method, where seagrass leaves were discretized into 4 segments, and ρ_{obst} (leaf bulk density) was set to 625 kg.m^{-3} (Auby, *pers. com.*). As indicated by Abdelrhman (2007), the drag coefficient (C_D) used here varies linearly from 1.2 for $\theta = 0$ (erected leaves) to 0 for $\theta = 90°$ (completely horizontally bent leaves).

For the runs performed using 3D formulations, the coefficient c_{lz} (eq. 7) was set to 0.2, roughly corresponding to the ratio between the thickness (t_e) and the width (w) of seagrass leaves. For the runs using 2D formulation, the coefficient $c_{z0,abd}$ (see section 2.2.2, Appendix A and Abdelrhman (2003) for further details) was calibrated and parameterized depending on leaf length (h_0), canopy height (h), total leaf density (n) and leaf width (w):

$$c_{z0,abd} = 2.6 \cdot \frac{h_0^2}{h^2 \cdot n_0 \cdot w} \qquad (12)$$

Since leaf density naturally varies with height, a height-dependant distribution of seagrass leaf density, derived from numerous field observations (Ganthy, 2011) was used (Figure 4). A summary of the experimental and model parameters is provided in Table 1.

For each test and flow regime, the model was run during 2 minutes (with a time-step of 0.025 seconds) to surpass the equilibrium state, which was typically reached after 1 minute on average. Results were outputted at 1 Hz over the last 30 seconds of the run. High frequency output is required to capture the turbulence and possible undulation of flexible obstructions and its interaction with hydrodynamics. Model results are then time-averaged to filter this high frequency variability. This post-processing strategy is common to all test cases.

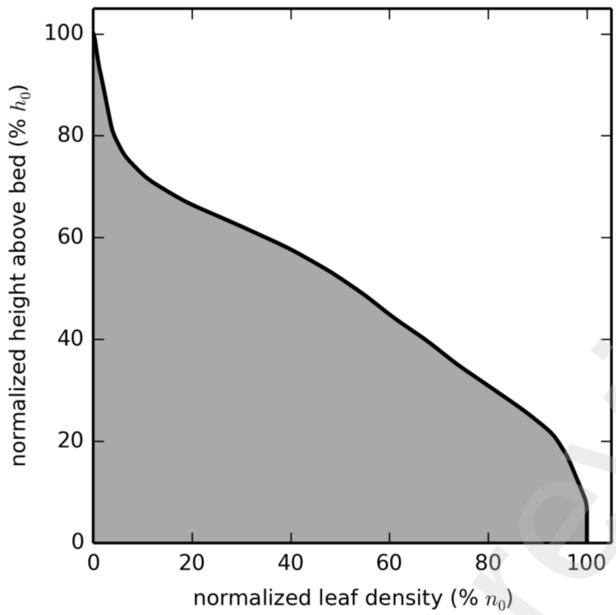

Figure 4: Vertical distribution of normalized leaf density from field observation (Ganthy, 2011) and used for the first set of numerical experiments.

Model settings					
Total length of the domain (m)	*1.5*				
Length of vegetation bed (m)	*0.9*				
Position of upstream edge of vegetation bed (m)	*0.5*				
Horizontal discretization (dx, m)	*0.05*				
Water depth (m)	*0.2*				
Vertical discretization (dz, m)	*0.005*				
z_0 *(m)*	*0.0002*				
Obstructions module parameters					
C_D *(-)*	*1.2*				
n_{seg} *(-)*	*4*				
ρ_{obst} *(kg.m*$^{-3}$*)*	*625*				
c_{lz} *(-)*	*0.2*				
$c_{z0,Abd}$ *(-)*	*Eq. 12*				
Tested velocities					
Identifier		*V1*	*V2*	*V3*	*V4*
U_∞ *(m.s*$^{-1}$*)*		*0.1*	*0.2*	*0.3*	*0.4*
Zostera noltei characteristics					
Identifier	*T1*	*T2*	*T3*	*T4*	*T5*
Total leaf density (n_0*, m*$^{-2}$*)*	*26650*	*34190*	*42540*	*80940*	*51080*
Leaf length (h_0*, m)*	*0.056*	*0.072*	*0.076*	*0.063*	*0.15*
Leaf width (w, m)	*0.00056*	*0.00058*	*0.00063*	*0.00082*	*0.00121*
Leaf thickness (t_0*, m)*	*0.0002*	*0.0002*	*0.0002*	*0.0002*	*0.0002*
Position of velocity measurement for model/data comparison					
0.45 m (from upstream edge of vegetated bed)					

Table 1. Model parameters and Zostera noltei characteristics for the ZNcase.

2.2.2. *Zostera marina* case (ZMcase)

This case aims to reproduce the straight flume experiments conducted by Lefebvre *et al.* (2010) in terms of velocity profiles for their Patch-1 to Patch-4. For each test, two free stream velocity values (V1 and V2, as listed in Table 2) were applied on *Zostera marina* patches across three patch lengths and two leaf densities (also listed in Table 2). Similarly to the ZNcase, all experimental flume conditions - including the dimensions of the flume and vegetated bed, water depth, seagrass characteristics and flow velocities - were replicated using a two-dimensional vertical (2DV) model configuration, which was run both using 3D and 2D modes.

The horizontal discretization (*dx*) was set to 0.05 m while 40 equidistant sigma layers (dz = 0.01 m) were defined for vertical discretization. Since this case was used to investigate the generic model feature for a different seagrass species, all model parameters used for the ZNcase were applied, except seagrass bulk density (ρ_{obst}) which was set to 700 kg.m^{-3}, according to Abdelrhman (2007). Model results were compared with flume data for profiles P2 to P5 (in Lefebvre *et al.*, 2010), which are located 0.15 m from the leading edge of the seagrass bed to 1.5 m downstream of the end of the vegetated bed, depending on its length (see Table 2 or Figure 1b in Lefebvre *et al.*, 2010).

In the absence of data on the vertical distribution of leaf density for *Zostera marina*, the distribution used for the ZNcase (Figure 4) was applied. Additionally, since Lefebvre *et al.* (2010) provided information on shoot density but not the mean number of leaves per shoot, which is required to compute the leaf density, the mean number of leaves per shoot (3.4) was derived from data collected in the Arcachon Bay (SW France) from 2007 to 2017 for the Europeean Water Directive Framework (Auby *et al.*, 2018).

Finally, for each test and flow regime, the model was run for 5 minutes (with a time-step of 0.025 seconds) to surpass the equilibrium state, which was typically reached after 3 minutes on average. Results were outputted at 1 Hz over the last 30 seconds of the run and then time-averaged.

Model settings				
Total length of the domain (m)			5	
Position of upstream edge of vegetation bed (m)			1.25	
Horizontal discretization (dx, m)			0.05	
Water depth (m)			0.4	
Vertical discretization (dz, m)			0.005	
z_0 *(m)*			0.0002	
Obstructions module parameters				
C_D *(-)*			1.2	
n_{seg} *(-)*			4	
ρ_{obst} *(kg.m^{-3})*			700	
c_{lz} *(-)*			0.2	
$c_{z0,Abd}$ *(-)*			eq. 12	
Tested velocities				
Identifier	V1		V2	
U_∞ *(m.s^{-1})*	0.1		0.2	
Test dependant parameters				
Identifier	Patch 1	Patch 2	Patch 3	Patch 4
Length of vegetation bed (m)	1.5	1.0	1.0	0.5
Total leaf density (n_0, m^{-2})	3300	3300	1980	3300
Leaf length (h_0, m)	0.284			
Leaf width (w, m)	0.004			
Leaf thickness (t_0, m)	0.00075			
Position of velocity measurements (m from upstream edge of vegetated bed)				
P2	0.15	0.15	0.15	0.15
P3	0.75	0.75	0.75*	0.75*
P4	1.35	1.35*	1.35*	1.35*
P5	2.0*	2.0*	2.0*	2.0*
**Indicates that profile is located downstream of vegetation patch*				

Table 2. Model parameters and Zostera marina characteristics for the ZMcase.

2.2.3. Mussel Long-Line case (MLLcase)

This case, inspired from numerical experiments of Delaux *et al.* (2011), aims to investigate the model's capability to simulate 3D velocities (free-stream velocity of 0.25 m.s^{-1}) in and around suspended shellfish structures (mussels long-line). A group of 5 long-lines (each 100 m in length, 1.5 m in width, and spaced 30 m apart), along with their associated droppers aligned with the flow, is simulated as rigid downward cylindrical obstructions. To minimize edge effects, the domain length and width were set to 800 and 400 m, respectively. The water depth was set to 5 m, and the droppers were considered to occupy half of this depth. The model resolution was set to 0.5 m horizontally (a compromise between grid size and computation time), and vertically it was discretized into 50 equidistant layers, resulting in a vertical resolution of 0.1 m. For each long-line, the dropper density (n_0) was set to 0.7 m^{-2} (and maintained constant vertically), and their diameter (d_0) was set to 0.25 m, consistent with the values used by Delaux *et al.* (2011) in their numerical experiments. The drag coefficient (C_D) was set to 1.2, consistent with values used in previous cases, and c_{lz} coefficient was set 0.8, a value determined to be applicable for cylinders by Uittenbogaard (2003). All model settings are summarized in Table 3. The model was firstly run using 3D formulations, and then using 2D formulations to investigate how the simplification (in term of depth-averaged velocities) affects the simulated results.

Finally, the model was run for 120 minutes (with a time-step of 0.25 seconds) to surpass the equilibrium state, which was reached after 100 minutes. Results were outputted at 0.2 Hz over the last 15 minutes of the run and then time-averaged.

Model settings	
Total length of the domain (m)	*800*
Domain length upstream long-lines (m)	*150*
Total width of the domain (m)	*450*
Horizontal discretization (dx, dy, m)	*0.5*
Water depth (m)	*5*
Vertical discretization (dz, m)	*0.1*
z_0 *(m)*	*0.0005*
Free-stream velocity (U_∞, $m.s^{-1}$)	*0.25*
Obstructions module parameters	
C_D *(-)*	*1.2*
n_{seg} *(-)*	*not used*
ρ_{obst} ($kg.m^{-3}$)	*not used*
c_{lz} *(-)*	*0.8*
$c_{z0,Abd}$ *(-)*	*not used*
Long-line characteristics	
Length of long-lines (m)	*100*
Width of long-lines (m)	*0.25*
Number of long-lines aligned to flow	*5*
Spacing between each long-line (m)	*20*
Droppers depth (h_0, *m*)	*2.5*
Droppers diameter (d_0, *m*)	*0.15*
Droppers density (n_0, m^{-2})	*0.7*

Table 3. Model parameters and long-line characteristics for the MLLcase.

2.2.4. Oyster-farm case (OYcase)

This case, inspired by the numerical experiments of Gaurier *et al.* (2011) aims to investigate the model's capability to simulate 3D velocities (free-stream velocity of 0.25 $m.s^{-1}$) in and around an oyster farming structure (comprising oyster tables and associated oyster bags). An oyster structure (100 m in length, 1.2 m in width) aligned with the flow is simulated using a combination of two types of obstructions: rigid upward cylindrical obstructions for the legs of the oyster table and a rigid O3D cylindrical obstruction for the oysters within the bags. To minimize edge effects, the domain length and width were set to 230 and 100 m, respectively. The water depth was set to 4 m, and the total height of the structure (table legs + oyster bags) was set to 0.82 m (0.72 m for table legs + 0.1 m for oyster bags). To optimize both grid resolution and computation cost, the horizontal grid discretization was not uniform in longitudinal (*dx*) and lateral (*dy*) directions. *dx* was set to 0.4 m, while *dy* was set to 0.15 m as higher resolution was needed to better simulate the two rows of table legs. The vertical dimension was discretized into 100 equidistant layers, resulting in a vertical resolution of 0.04 m. For both table legs and oyster bags, obstructions characteristics (i.e. legs diameter, height, and density, oyster diameter, density, and height of a bag) were set to values representatives to those found in realistic oyster farming structures. However, the bag itself, generally corresponding to a plastic net with variable meshes sizes (from 2 to 14 mm), was neglected. The model settings and parameters are summarized in Table 4. Similarly to the MLLcase, the model was first run using 3D formulations and then using 2D formulations to investigate how the simplification (in term of depth-averaged velocities) affects the model's predictions.

Finally, the model was run for 60 minutes (with a time-step of 0.25 seconds) to surpass the equilibrium state, which was reached after 40 minutes. Results were outputted at 0.2 Hz over the last 15 minutes of the run and then time-averaged.

Model settings	
Total length of the domain (m)	*230*
Domain length upstream oyster table (m)	*100*
Total width of the domain (m)	*100*
Horizontal longitudinal discretization (dx, m)	*0.4*
Horizontal lateral discretization (dy, m)	*0.15*
Water depth (m)	*4*
Vertical discretization (dz, m)	*0,04*
z_0 *(m)*	*0.005*
Free-stream velocity $(m.s^{-1})$	*0.25*
Obstructions module parameters for table legs	
C_D *(-)*	*1.2*
n_{seg} *(-)*	*not used*
ρ_{obst} $(kg.m^{-3})$	*not used*
c_{lz} *(-)*	*0.8*
$c_{z0,Abd}$ *(-)*	*not used*
Table legs characteristics	
Domain length upstream oyster table (m)	*100*
Length of table (m)	*100*
Width of legs, each side (m)	*0.15*
Legs height (h_0, *m)*	*0.72*
Legs diameter (d_0, *m)*	*0.016*
Legs density (n_0, *m-2)*	*1*
Obstructions module parameters for oyster bags	
C_D *(-)*	*1.2*
n_{seg} *(-)*	*not used*
ρ_{obst} $(kg.m^{-3})$	*not used*
c_{lz} *(-)*	*0.8*
$c_{z0,Abd}$ *(-)*	*not used*
Obstruction related parameters for oyster bags	
Length of table (m)	*100*
Width of oyster bags (m)	*1.2*
Occupied height above the bed (m)	*0.72 to 0.82*
Oyster diameter in bag (d_0, *m)*	*0,04*
Oyster density in bags (n_0, *m-2)*	*120*

Table 4: *Model parameters and obstruction characteristics for the OYcase.*

2.3. Settings for sensitivity analysis

A sensitivity analysis was conducted for the ZNcase. This case allows for testing most of the model parameters, including those dedicated to flexible obstruction type, and encompasses a broader panel of flow conditions and obstructions characteristics. The model parameters and methods used to describe obstructions were grouped into four main groups:

- (1) main model parameters: bottom roughness length (z_0), obstruction drag coefficient (C_D), number of segments (n_{seg}) and obstruction bulk density (ρ_{obst}) for canopy height computation using the Abdelrhman's procedure, the coefficient c_{lz} for typical size of eddies (Eq 7) and the coefficient $c_{z0,abd}$ used for theoretical computation of velocity profiles using 2D formulations.
- (2) obstruction's variables: the total leaf density (n_0), leaf length (h_0), leaf width (w) and leaf thickness (t_0).
- (3) methods used for obstruction description: using cylinder-like obstructions instead of parallelepiped-like (*Cyl*), without using vertical-varying leaf density (*Cst n(z)*) and empirical parameterization of canopy height (*h param*) instead of following the Abdelrhman's procedure.
- (4) domain discretization: horizontal (dx) and vertical (dz) discretizations.

Each model parameter or method was tested separately. For the main model parameters (1) and obstruction variables (2), each parameter was tested by changing its value by ± 50% while keeping the others constant (refer to Table 1). For domain discretization (4), dx and dz were multiplied by two (corresponding to dx_2 = 0.1 m and dz_2 = 0.01 m, respectively) or four (corresponding to dx_4 = 0.2 m and dz_4 = 0.02 m, respectively).

2.4. Statistics for numerical solution evaluations

Firstly, for each velocity profile (for ZNcase and ZMcase), the root mean square error (*RMSE*, in m.s^{-1}) and the normalized root mean square error (NRMSE, in %) were computed as follow:

$$RMSE = \sqrt{\frac{\sum_{j=1}^{N}\left(U_{\mathrm{mod}(j)} - U_{mes(j)}\right)^2}{N}} \tag{13}$$

$$NRMSE = 100 \cdot \sqrt{\frac{\sum_{j=1}^{N}\left(\frac{U_{\mathrm{mod}(j)} - U_{mes(j)}}{U_\infty}\right)^2}{N}} \tag{14}$$

where U_{mod} and U_{mes} are the simulated (nearest grid cell from observation position) and measured velocities respectively, U_∞ is the free-stream velocity, j represents the considered vertical point of the profile and N is the number of data point in the considered profile. For all cases, simulated velocity profiles are linearly interpolated on data measured at different heights above the bed.

In order to perform model-to-model comparison, for each simulation (i.e. tested parameter or method), the normalized difference of the normalized root mean square error ($\Delta NRMSE_{norm}$, expressed as a percentage of the reference run) was computed as follow:

$$\Delta NRMSE_{norm} = 100 \cdot \frac{NRMSE_{Run} - NRMSE_{REF}}{NRMSE_{REF}} \tag{15}$$

where $NRMSE_{Run}$ is the global normalized root mean square error (accross all tests: T1-T5 and V1-V4) resulting from the tested parameter change, and $NRMSE_{REF}$ is the global normalized root mean square error for the reference simulation (for the ZNcase). Therefore, positive values indicate that the model accuracy is lower compared with the reference simulation.

3. Results

3.1. ZNcase

A comparison between simulated and measured velocity profiles is given in Figure 5, and a summary of the statistical parameters used for model evaluation is presented in Table 5. Velocities simulated using the 3D formulations align closely with the measurements (Figure 5), both in terms of velocity reduction within the canopy and the development of the shear layer at the top of canopy. The normalized root mean square error (*NRMSE*) ranges from 7.1% (for T5V4) to 22.2% (for T3V1), with an overall value of 11.5% (Table 5). For all seagrass characteristics (T1-T5), the correlation coefficients are at least 0.98. Compared with results from the previous version of the model presented in Kombiadou *et al.* (2014), the current model more accurately predicts the velocity reduction in the upper region of the canopy. Kombiadou *et al.* (2014) indicated an underestimation of the velocity reduction leading to a milder velocity gradient at the top of the canopy, whereas the present model results are significantly closer from measurements. This improvement is likely due to a more physical approach of canopy height computation (i.e. Abdelhrman's procedure instead of an empirical polynomial formulation).

Considering velocities simulated using the 2D formulations (theoretical computation of velocity profiles, see section 2.1.2), *NRMSE* values range from 7.6% (T1V2) to 31.1% (T4V1), with an overall value of 18.1%. This is higher than values obtained using the 3D formulations (Figure 5). In general, for denser seagrasses (mainly for T4 and T5 tests) the velocity reduction within the canopy is underestimated, particularly at low velocities. Simulated velocities above the canopy are lower than observed, showing a logarithmic shape from the top of the canopy to the water surface. Although this theoretical method partially failed to reproduce the shear layer, the correlation coefficients are always above 0.95 (Table 5). Near-bed velocities, which are used to compute the bottom-shear stress in the sediment transport module, are generally well reproduced and are considered very satisfactory given the high level of simplification of the dynamics.

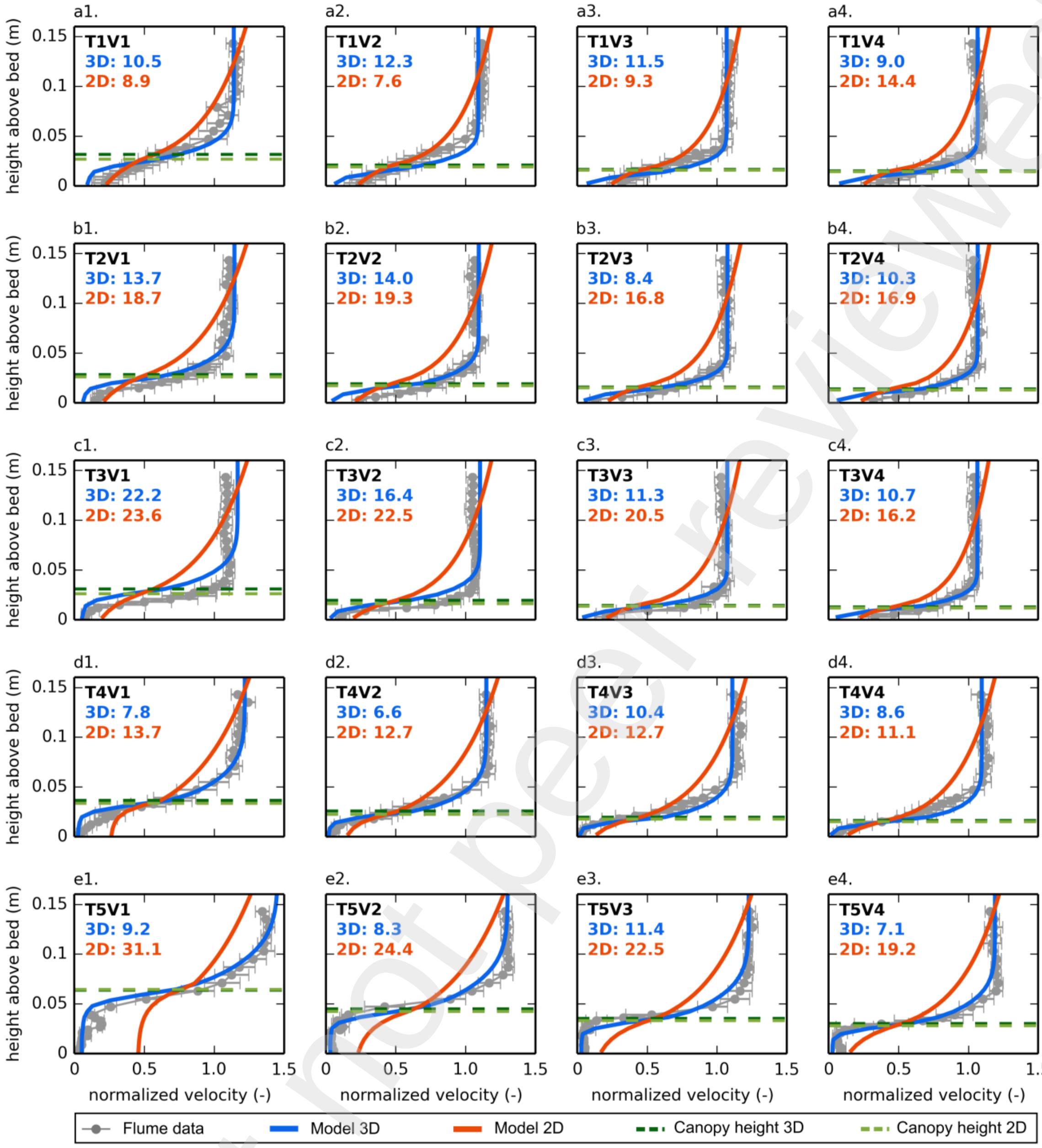

Figure 5: Measured and simulated velocity profiles for the ZNcase for the five seagrass characteristics (T1 to T5) and the four velocity treatments (V1 to V4) at 0.45 m from the upstream edge of the vegetated patch. Measured velocities (grey circles) are presented with their standard-deviation, velocities simulated using 3D formulations are dark blue (with their associated predicted canopy height in dark green), while 2D formulations are in grey-blue (with their associated predicted canopy height in light green); the normalized root mean square errors (%) are also indicated for both the two formulations.

Tests		T1	T2	T3	T4	T5	Total
R^2	3D	0.98	0.98	0.98	0.99	0.99	0.98
	2D	0.98	0.96	0.95	0.98	0.96	0.96
RMSE ($m.s^{-1}$)	3D	0.024	0.022	0.029	0.019	0.021	0.023
	2D	0.025	0.040	0.045	0.028	0.051	0.042
NRMSE (%)	3D	10.9	11.9	15.8	8.5	9.1	11.5
	2D	10.4	17.9	20.9	12.6	24.7	18.1

Table 5: Synthesis of statistics values between measured simulated velocities obtained for the ZNcase: correlation coefficient (R^2), root mean square error (RMSE) and normalized root mean square error (NRMSE).

3.2. ZMcase

In this case, four different eelgrass patches were simulated at two velocities using both 3D and 2D formulations. Simulated velocity profiles were compared with those measured by Lefebvre *et al.* (2010) in their flume at four locations. To illustrate model results, an example of comparison between simulated and measured velocity profiles is provided in Figure 6 for Patch-1 (high eelgrass density) for the two free stream velocity values (0.1 and 0.2 $m.s^{-1}$). The statistical results obtained for all the four eelgrass patches and the two free stream velocity values are summarised in Table 6.

Regarding results obtained using the 3D formulations, the *NRMSE* ranges from 11.4% (Patch-1, P2) to 19.0% (Patch-4, P2), with an overall value around 15.4% considering all profiles located within the seagrass bed (Table 6). The correlation coefficient also exhibits high values, generally over 0.9, for all profiles located within seagrass beds. However, the model appears less accurate when considering profiles located downstream of the seagrass bed (profile P5 for all tests, P4 for test Path-2, Patch-3 and Patch-4, and P3 for test Patch-4). Even though the velocity inside the canopy is slightly underestimated for profiles P3 and P4, respectively located at 0.75 and 1.35 m downstream from the edge of the seagrass bed, the main vertical pattern of the flow along the vegetation patch is well simulated with 3D formulations (Figure 6 a1-a3 and b1-b3). In contrast, for profile P5 (0.5 m downstream from the vegetation patch, Figure 6 a4 and b4) the near-bed velocity attenuation is underestimated by the model, possibly due to the length of seagrass leaves (0.28 m), where bending may extend the distance over which near-bed velocity is attenuated.

Regarding simulated velocity profiles using 2D formulations, similarly to the ZNcase, both RMSE and R^2 values (Table 6) indicate that the model is less accurate than using 3D formulations. The less accurate results are obtained for profiles located downstream the seagrass patch. In this case no obstructions are present and velocity profile simply consists in a classical Law of the Wall (Figure 6 a4 and b4). Furthermore, as vertical advection is not taken into account in 2D, the horizontal flow pattern at the leading edge of the seagrass patch cannot be reproduced by the model, leading to an underestimation of near-bed velocities for the profile P2 (Figure 6 a1. and b1.). However, considering profiles P3 and P4, located further inside the seagrass patch, results remain very satisfactory (overall NRMSE of 19.7 and 16.1% and R^2 of 0.98 and 0.97 respectively, Table 6, Figure 6 a2, a3, b2 and b3).

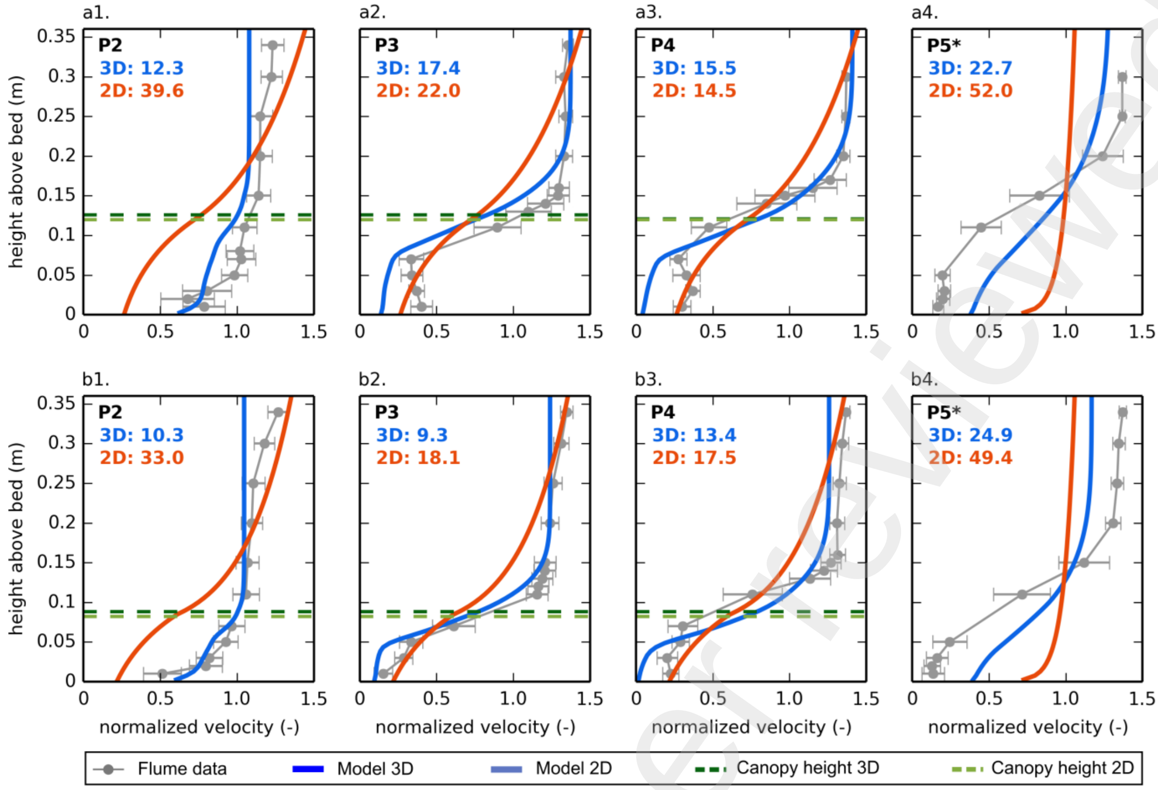

*Figure 6: Measured and simulated velocity profiles for the ZMcase for the Patch-1 and the two velocity treatments (V1, upper panel and V2, lower pannel) for the different profile locations (P2 to P5). P2 to P4 are profiles measured within the patch, while the profile P5, marked by a *, was measured 0.5 m downstream the end of the seagrass patch. Measured velocities (grey circles) are presented with their standard-deviation, velocities simulated using 3D formulations are dark blue (with their associated predicted canopy height in dark green), while those simulated using 2D formulations are in grey-blue (with their associated predicted canopy height in light green); the normalized root mean squared errors (%) are also indicated for both the two formulations.*

	Profiles		P2	P3	P4	P5
Patch-1	R^2	3D	**0.97**	**0.99**	**0.97**	0.96*
		2D	**0.85**	**0.96**	**0.97**	0.66*
	RMSE ($m.s^{-1}$)	3D	**0.017**	**0.018**	**0.021**	0.036*
		2D	**0.053**	**0.029**	**0.025**	0.075*
	NRMSE (%)	3D	**11.4**	**14.0**	**14.4**	23.9*
		2D	**36.6**	**20.2**	**16.1**	50.7*
Patch-2	R^2	3D	**0.87**	**0.98**	0.96*	0.92*
		2D	**0.84**	**0.97**	0.70*	0.70*
	RMSE ($m.s^{-1}$)	3D	**0.027**	**0.021**	0.030*	0.039*
		2D	**0.053**	**0.028**	0.063*	0.063*
	NRMSE (%)	3D	**18.0**	**15.6**	20.1*	26.1*
		2D	**38.5**	**19.5**	42.1*	42.6*
Patch-3	R^2	3D	**0.94**	**0.97**	0.98*	0.96*
		2D	**0.87**	**0.97**	0.83*	0.83*
	RMSE ($m.s^{-1}$)	3D	**0.018**	**0.026**	0.019*	0.024*
		2D	**0.047**	**0.025**	0.043*	0.042*
	NRMSE (%)	3D	**12.0**	**18.6**	12.4*	16.8
		2D	**33.5**	**19.3**	30.4*	30.4*
Patch-4	R^2	3D	**0.96**	0.97*	0.95*	0.95*
		2D	**0.82**	0.73*	0.77*	0.83*
	RMSE ($m.s^{-1}$)	3D	**0.020**	0.023*	0.026*	0.033*
		2D	**0.052**	0.037*	0.049*	0.058*
	NRMSE (%)	3D	**19.0**	15.8*	17.4*	17.1*
		2D	**32.9**	36.1*	33.3*	27.3*
Total	R^2	3D	**0.93**	0.97 (**0.98**)	0.96 (**0.97**)	0.94*
		2D	**0.84**	0.89 (**0.96**)	0.82 (**0.97**)	0.74*
	RMSE ($m.s^{-1}$)	3D	**0.022**	0.023 (**0.022**)	0.025 (**0.021**)	0.033*
		2D	**0.052**	0.037 (**0.027**)	0.049 (**0.025**)	0.058*
	NRMSE (%)	3D	**15.5**	16.1 (**16.2**)	16.3 (**14.4**)	21.2*
		2D	**35.5**	24.8 (**19.7**)	31.9 (**16.1**)	38.3*

*Table 6: Synthesis of statistics values between measured simulated velocities obtained for the ZMcase: correlation coefficient (R^2) and root mean square error (RMSE). For the different patchs, values in bold indicates that the corresponding velocity profile was located within the seagrass patch, while those marked by a * indicates that the corresponding velocity profile was located downstream the end of the seagrass patch. Considering total values, the main value corresponds to the overall value and the value in bold between parenthesis corresponds to the value computed only within the seagrass patch.*

4. Discussion

4.1. Model reliability and sensitivity

Compared to results obtained by Kombiadou *et al.* (2014), this new version of the OBSTRUCTIONS module slightly improves the simulation of vertical velocity profiles accross all tests. However, for tests with highly developed seagrass beds (tests T4 and T5), the results demonstrate a significantly better model capability to simulate velocities in the upper part of the canopy, with a more developed shear layer. In the previous model version (Kombiadou *et al.*, 2014) the velocity was overestimated near the top of the canopy for tests with high leaf densities. This improvement can be attributed to (1) the better representation of seagrass leaf morphology (parallelepipeds instead of cylinders) and (2) the better simulation of canopy height (physical computation based on balance of forced instead of a polynomial empirical formulation), as discussed hereinafter.

Results from the sensitivity analysis (ZNcase) are summarized in Figure 7a and 7b for the 3D and 2D formulations, respectively. Overall, the model appears more sensitive to the tested parameters and methods using 3D formulations than using 2D ones, exhibiting a similar pattern but different intensities. Although 11 parameters, variables and methods (excluding horizontal and vertical model resolution) are needed to setup the OBSTRUCTIONS module, the latter is mostly affected by parameters/variables/methods representing the obstructions. Specifically, the model appears very sensitive to methods: using cylinders instead of parallelepipeds, using parameterized canopy height instead of physical formulation based on forces, and the use of a constant vertical distribution of obstructions instead of a measured one. Regarding obstructions characteristics and parameters, the model prediction appears mainly affected by leaf length (h_0) and the obstructions bulk density (ρ_{obst}), and to a lesser extent by the obstruction's drag coefficient

(C_D), which are key parameters for canopy height computation using balance of forces. The model's behaviour is consistent with previous studies. Boothroyd *et al.* (2016) demonstrated the importance of accurately representing complex plant morphology in hydraulic models. Furthermore, in their multi-specific flume and modelling experiments, Weitzman *et al.* (2015) highlighted the important role of the vertical distribution of biomass on the shape of velocity profile. Finally, compared with leaf density (n_0) which has a very limited impact on model prediction, the computed canopy height strongly affects model reliability. This is in agreement with results from Dijkstra and Uittenbogaard (2010), who demonstrated that obstructions flexibility has a greater impact on flow reduction within the canopy than element density, both in their flume and numerical experiments.

Consequently, when simulating flow through flexible obstructions (*i.e.* vegetation), the use of Abdelhrman's (2007) method appears to be the best approach to properly compute canopy height. However, this method is only applicable to very flexible obstructions, since element elasticity is not taken into account. Introducing an elasticity term based on the elasticity modulus and moment of inertia within the bending algorithm would improve flow prediction for obstructions with characteristics ranging between fully rigid to fully flexible. Thus, as stated by Dijkstra and Uittenbogaard (2010), the model would then require additional inputs of obstructions properties (such as the elasticity modulus). However, such properties are neither easily nor usually measured for seagrass species and the rare studies dealing with measurements (or proxy) of those parameters highlighted significant spatio-temporal variability (Soissons *et al.*, 2017).

Apart from variables and methods describing obstructions, the model is only sensitive to two parameters: the drag coefficient (C_D) which can be calibrated and the obstruction bulk density (ρ_{obst}) which can be obtained from measurements. Otherwise these parameters can be picked up in the literature. Values for the drag coefficients usually range from 1 to 1.5. In our model, the use of an intermediate value of 1.2 provides reliable results, and no additional calibration was performed. An improvement of the model, when applied to seagrass meadows, would be to parameterize time-varying drag coefficient and obstruction bulk density in order to account for seasonal epiphytes growth on seagrass leaves, as epiphytes are likely to modify both the leaf drag and bulk density.

Due to the quasi-absence of calibration requirements to accurately simulate the seagrass-flow interactions, it can be expected that applying the model to other types of obstructions would provide satisfactory results with minimum calibration effort, as long as obstructions are properly described.

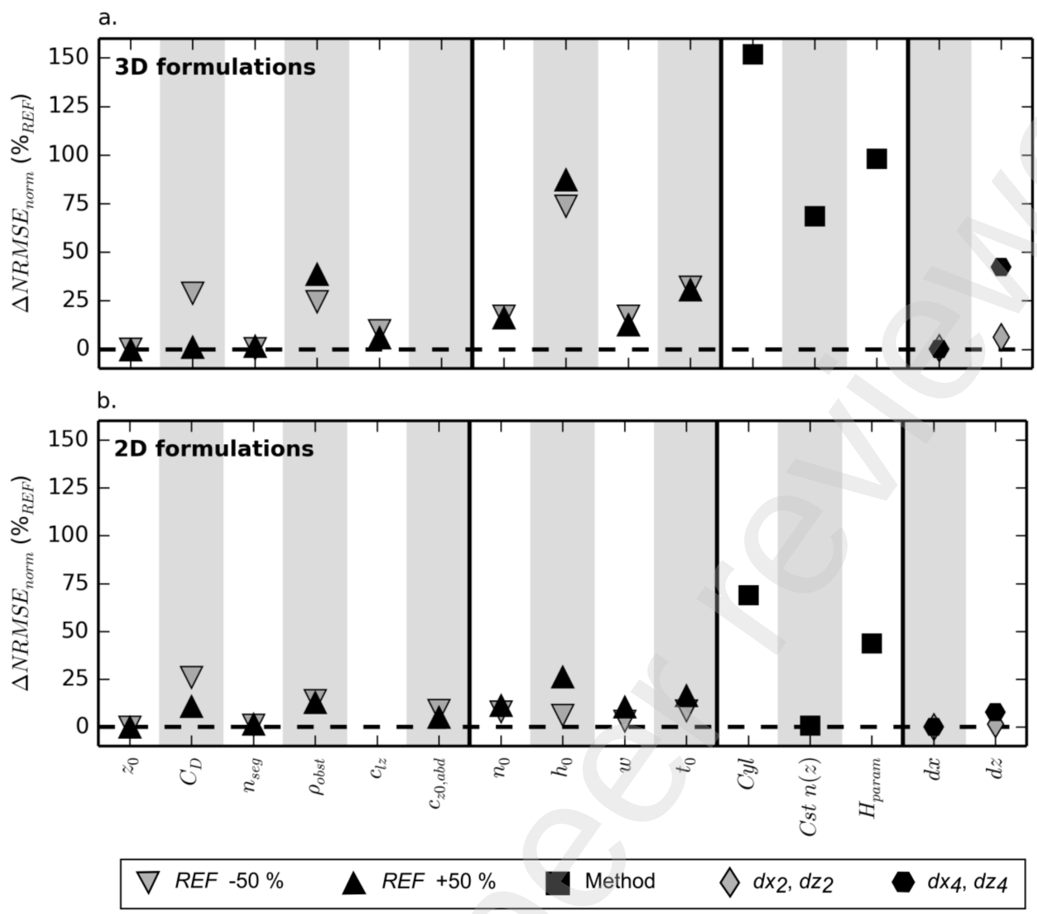

Figure 7: Results of the model sensitivity analysis performed on Obstructions module parameters (from C_D to $c_{z0,abd}$), obstructions characteristics (from n_0 to t_0), method describing obstructions (Cyl and Cst (z)) and grid discretization (dx and dz), in terms of normalized changes in normalized root mean square error ($\Delta NRMSE_{norm}$) for (a.) 3D formulations and (b.) 2D formulations. Notice that $c_{z0,abd}$ is not used by 3D formulations, while c_{lz} is not used by 2D formulations.

Finally, in contrast to horizontal discretization (*dx*), for which the sensitivity is negligible, the model demonstrated a significant sensitivity to vertical discretization, particularly when the vertical resolution was reduceded by a factor of four (*dz4*), *i.e.* from 5 mm to 20 mm. The effect of vertical discretization is illustrated in Figure 8 for two contrasting seagrass characteristics (see Table 1), using both 3D and 2D formulations. The impact of vertical resolution on the velocity profile appears to be stronger for 3D formulations than for 2D ones.

The vertical discretization needs to be carrefully defined depending on processes to be investigated (*e.g.* shear layer) and/or on the purpose of the model application (*e.g.* sediment dynamics). However, few comments can be made: (1) it is advisable to define discretization to ensure at least two layers within the canopy, (2) the first bottom layer should be as thin as possible to obtained more reliable bottom velocities for bottom shear stress computation in dynamics modelling, (3) refining the vertical grid in the shear layer at the top of the canopy allows for an increase in the model time-step due to lower velocity gradients between successive layers.

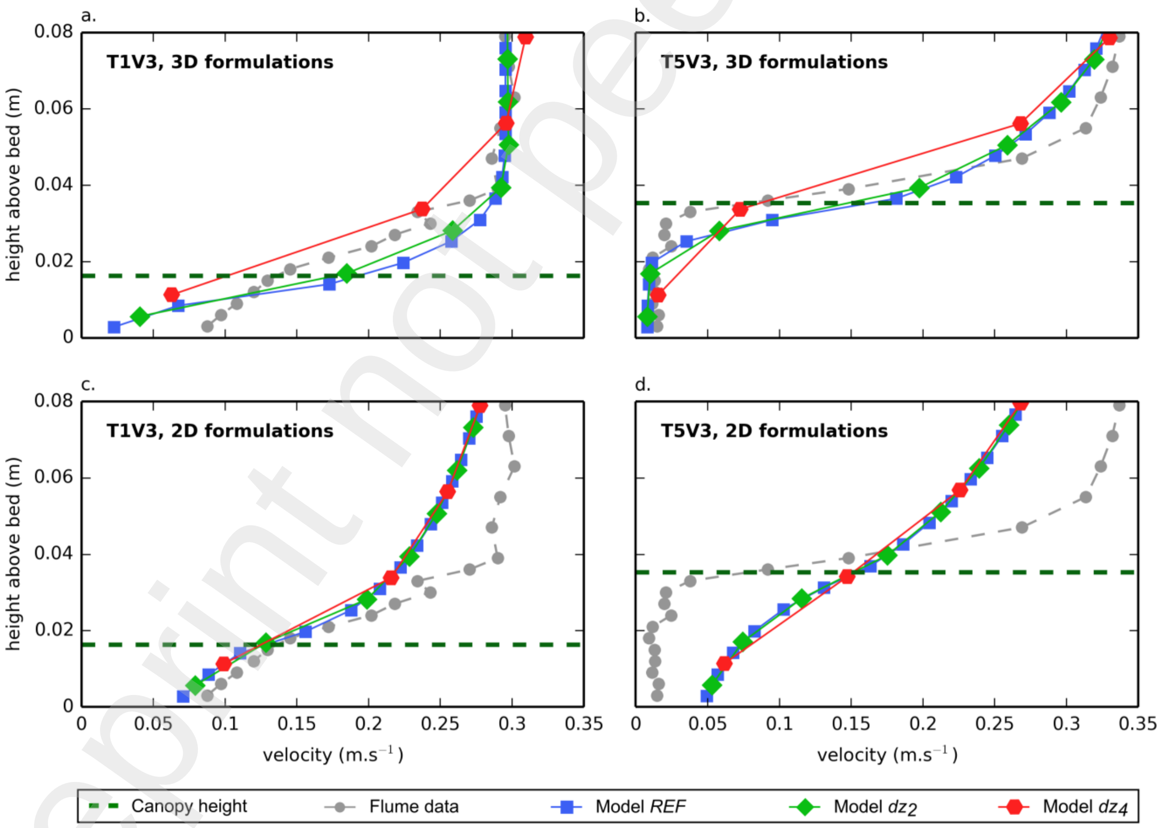

Figure 8: Comparison of measured and simulated velocity profiles depending on model vertical resolution using 3D (a. and b.) and 2D (c. and d.) formulations for two contrasted seagrass development stage, test T1 (winter development, a. and c.) and T5 (summer development, b. and d.).

4.2. Application to different obstruction types

Physical obstructions in coastal systems come in various forms, ranging from various types of vegetation (e.g., seagrass meadows, seaweeds or mangroves) to human-made structures like aquaculture facilities (oyster and mussels farms), pontoons and piles. The present model was specifically designed to be able to represent most of these obstructions. This generic feature is illustrated and discussed below using two distinct examples of anthropogenic obstructions found in coastal systems: mussel long lines and oyster farms.

4.2.1. Application to mussel long-lines farming (MLLcase)

Mussel Long-Lines (MLL) are transectstructures with regularly-spaced vertical dropper lines from the surface, where mussels attach and grow. In the Delaux experiment, their typical dimensions are 0.5 m width and 2.5 m vertical lines. This type of structures is used worldwide as mussel farming technique (Plew *et al.*, 2005; Plew, 2010; Delaux *et al.*, 2011; McKindsey *et al.*, 2011).

MLL have a significant impact on depth-averaged current velocity along the long-line, regardless of whether a 3D or 2D formulation is investigated. Our simulations show a reduction of the depth-averaged velocity by up to 0.4 U_∞ close the MLL (Figure 9). A wake clearly develops along the line and downstream, showing a flow velocity reduction of 0.6 U_∞ 30 m downstream from the line's edge, and still reaching 0.8 U_∞ 50 m downstream from the structure. Additionally, there is a flow velocity acceleration between the lines of 1.2 U_∞ in 2D. These results, both in terms of velocity reduction and wake spatial distribution are in good agreement with results from Delaux *et al.* (2011). However, depth-averaged or 3D approaches show some discrepancies, either on the absolute velocity reduction, the inter-line acceleration or the wake spreading, which is wider in 2D than in 3D. Lateral velocity is stronger in 2D than in 3D, especially at the upstream and downstream edges of the long-line.

This difference can be attributed to the vertical flow deflection which is not taken into account in 2D. In the 2D model, most of the flow is laterally deflected on both sides of long-lines, while in 3D, the flow is deflected both vertically (below the long-line) and laterally.

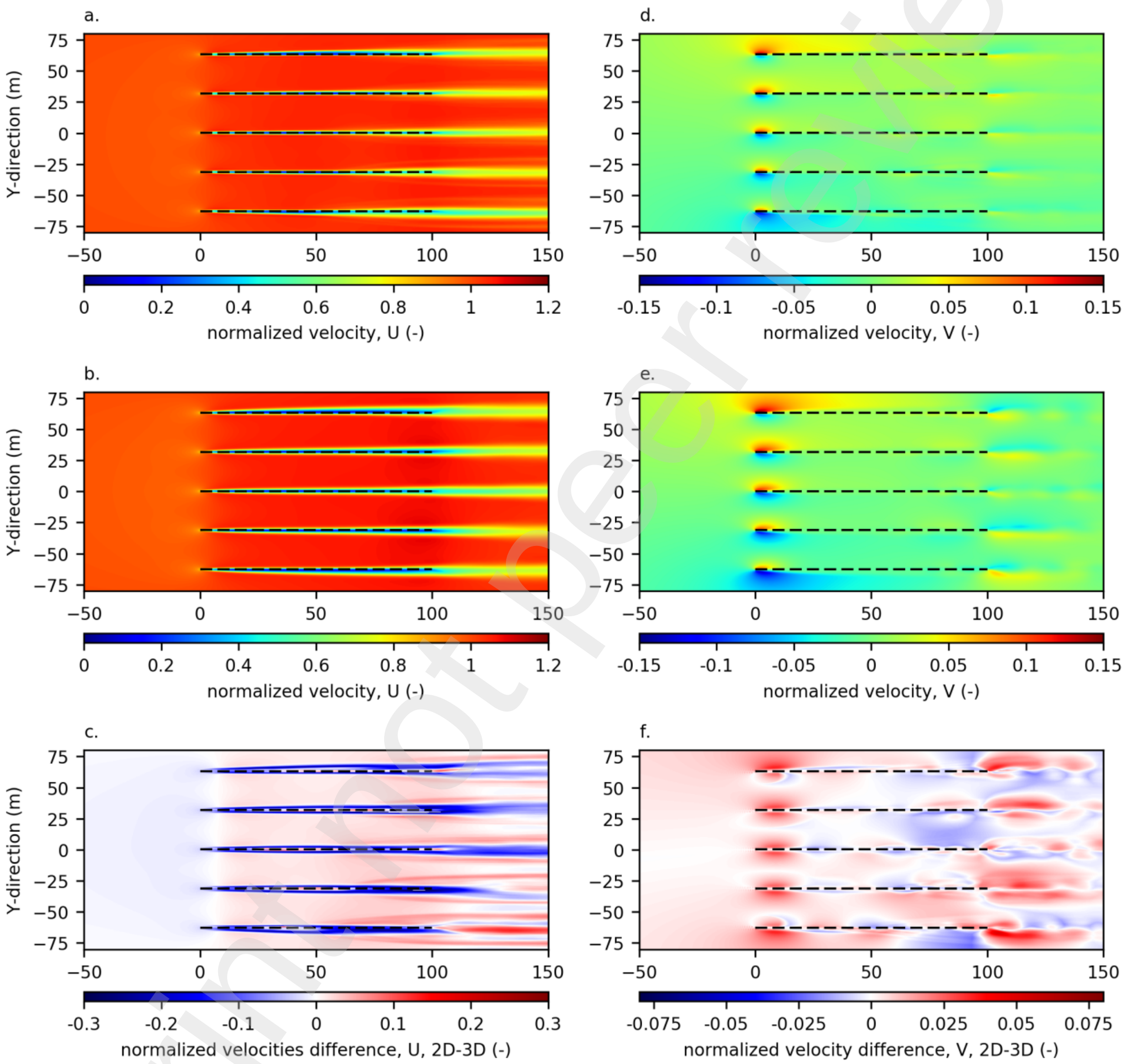

Figure 9: Depth-averaged normalized velocities simulated for the MLLcase using 3D (a. and d.) and 2D (b. and e.), as well as the differences of normalized velocities between 3D and 2D simulations (c. and f.), for the longitudinal velocity component (U, left panel, a., b. and c.) and for the lateral velocity component (V, right panel, d., e. and f.). Long-line locations are indicated by black dotted lines.

The full 3D model reveals detailed consequences of the presence of MLL on the 3D velocity field (Figure 10). The flow velocity is abruptly reduced by at least 0.2 U_∞ within the MLL canopy, showing values that are close but still larger values than the velocity reduction observed *in-situ* by Plew *et al.* (2005). These discrepancies in magnitude could be attributed to differences in geometry configuration between *in-situ* experiments and numerical experiments, as well as the challenges in recording reliable measurements within the farm (Plew *et al.,* 2005). In our numerical configuration, a significant drop in velocity is observed below the canopy down to the bottom, where the flow velocity reduction ranges from 0.7 U_∞ to 0.9 U_∞. This low-flow area would be favorable for pseudofaeces sedimentation, as observed *in-situ* (Mc Kinsdey *et al.*, 2011). Due to the development of wake turbulent structures along the long-line, the velocity tends to weakly accelerate again in the latter half of the long-line and more significantly below the canopy. Velocity increases rapidly downward without reaching the upstream velocity, even after 200 m, as also highlighted by Delaux *et al.* (2011).

Although depth-averaged velocity discrepancies between 2D and 3D formulations remains relatively low, the geometry of long-lines lead to complex 3D flow structures. This has direct impacts on sediment dynamics and biodeposition patterns. It is also highly recommended to use 3D formulations in such applications.

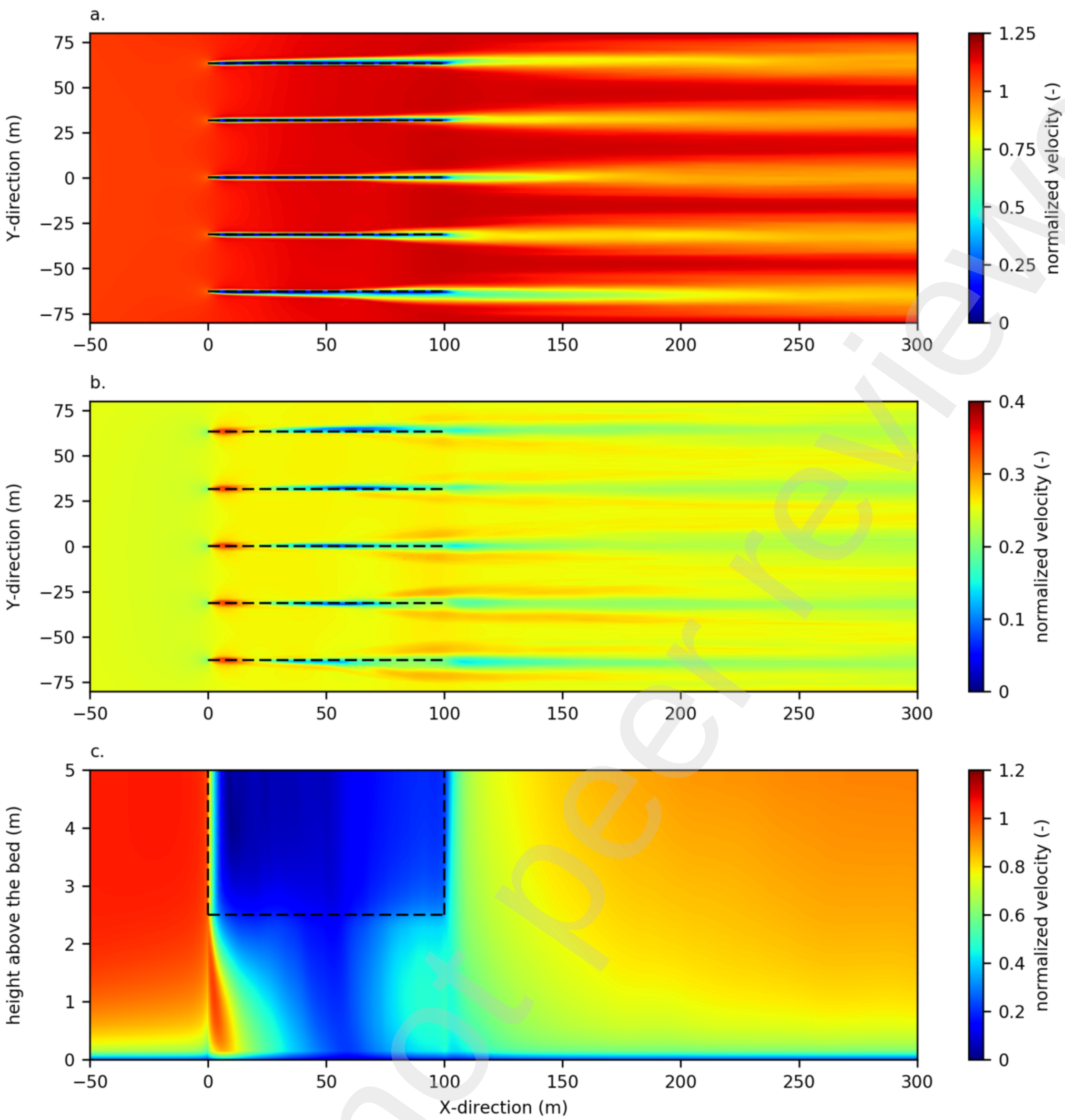

Figure 10: Normalized velocities simulated for the MLLcase using 3D formulations: (a.) upper view of surface velocities, (b.) upper view of bottom velocities, and (c.) side view of velocities at Y=0 (i.e. within the central long-line). Long-line locations are indicated by black dotted lines.

4.2.2. Application to oyster tables (OYcase)

Oysters are generally cultivated using long-lines, similar to those discussed above for mussels, or they are elevated above the bed using oyster table arrays organized in blocks covering several squared kilometres in intertidal areas (Kervella *et al.*, 2010). For instance, in the Mont Saint-Michel Bay in France, each table array is 0.7 m high above the bed, 1 m wide, and 100 m long. Oysters are enclosed in meshed bags (0.1 m high) attached horizontally to the table. As described in section 2.2.4, the generic obstruction model was configured to represent a 100 m long table array, similarly to the numerical setup of Gaurier *et al.*, (2011) and closely resembling the experimental setup of Kervella *et al.* (2010), except the table array length, which was necessarily shorter due to limitation imposed by the experimental facility dimension.

The obstruction element parameters (table and oyster bags dimensions) were set according to nature, without further specific calibration. Model results show very good qualitative and quantitative agreement with both the laboratory experiment results from Kervella *et al.* (2010) and the numerical experiment from Gaurier *et al.* (2011, Figure 11). Velocity within oyster bags is strongly reduced compared to the free-stream velocity U_∞. This reduction tends to increase from 0.4 U_∞ at the upstream edge to reach 0.15 U_∞ roughly 25 m inside the oyster bags (Figure 11a). Below table, a boundary layer can develop caused by oyster bag drag and merges with the bottom boundary layer 20 m downstream the table leading edge. Over this 20 m distance, flow velocity below tables rapidly drops to reach 0.2 U_∞ and stabilizes. Similarly, a boundary layer develops above the table, leading to a decrease in velocity to 0.5 U_∞ winthin 1 m around the structure at the trailing edge (Figure 11e). This decrease in velocities around and below oyster table, together with high settling velocity of pseudofaeces, has evident implication on siltation and sediment accumulation nearby these structures, as observed in Marennes-Oléron Bay (Sornin, 1981).

2D simulations were also conducted, and the main results and conclusions (Appendix C) are similar to the MLLcase: model results in 2D are broadly similar to 3D, while the wake around the table is more developed and flow velocity reduction is slightly stronger.

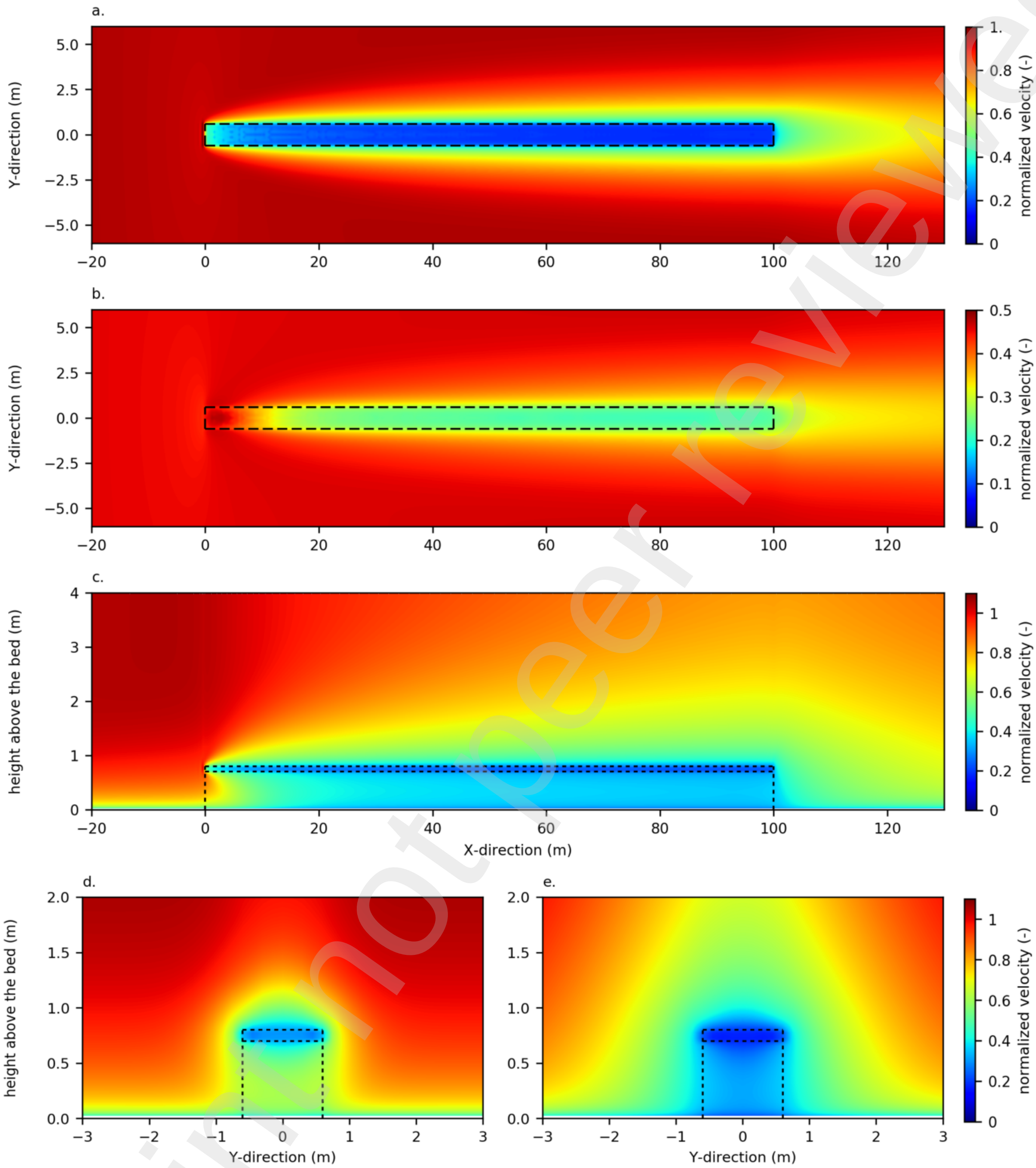

Figure 11: Normalized velocities simulated for the OYcase using 3D formulations: (a.) upper view of velocities at 0.75 m above the bed (i.e. at half height of oyster bags), (b.) upper view of bottom velocities, (c.) side view of velocities at Y=0 m (i.e. at half width of the oyster table), and cross view of velocities at X=2 m (d., 2 m downstream the leading edge of the

oyster table) and at X = 98 m (e., 2 m upstream the end of the oyster table). Table locations (bags and tables legs) are indicated by black dotted lines.

4.3. Toward regional scale modelling

As demonstrated above, the OBSTRUCTIONS module is applicable and reliable for simulating various type of flow-obstruction interactions at the obstruction scale, under steady or unsteady forcing conditions. The main ambition is to upscale this module to regional scale (bays, lagoons, estuaries) over annual to decadal scales, in order to evaluate the impact of anthropogenic and natural obstructions on the hydrodynamics, the sediment dynamics, and ultimately, ecosystem dynamics in the context of global change. While the OBSTRUCTIONS module is technically applicable to a regional scale, upscaling to larger grid cell (O(100 m)) and longer running time (O(1 y)-O(10 y)) remains challenging and require adaptations to overcome current limitations due to vertical and horizontal model description. The discussion will be illustrated using the *Zostera noltei* meadows-hydrodynamics interactions in the Arcachon lagoon. However the discussion can be generalized to any other type of obstructions.

4.3.1. Upscaling challenge #1: the vertical description

The primary criterion for an operational regional model is to utilize the largest time step and the coarsest affordable vertical description to save computation time without a significant compromise on process representation and result quality.

The sensitivity analysis of the 3D formulation presented above recommends carefully defining the vertical sigma layer distribution. This includes using at least 2 vertical layers to describe obstructions, establishing a thin first sigma layer to efficiently calculate bottom velocity, and optionally refining the vertical mesh around the shear layer near the obstructions. As *Zostera noltei* meadows mainly grow in intertidal areas, where water depth can reach 2 to 3 m at highest spring tides, optimizing the sigma layer distribution accordingly may not be straightforward. The stability of the OBSTRUCTIONS module in full 3D requires reducing computation time steps (by 2 to 5) compared to the model without obstructions, likely due to stronger horizontal and vertical velocity gradients near the obstruction elements. The need for shorter time steps makes long-term simulations less affordable.

Using mixed 2D/3D calculations can be a solution to expedite model computation but with significant consequences on simulated processes. As previously mentioned, *Zostera noltei* is found in intertidal areas. Therefore, increasing the 2D/3D water depth threshold to the deepest vegetation depth at high spring tide (e.g., 2-3m in the Arcachon lagoon) implies solving all dynamics (hydrodynamics, obstruction, and other processes) in 2D, while deeper areas like tidal channels and offshore areas will still be computed in 3D. While this option can significantly reduce computation time, it treats all intertidal dynamics as vertically mixed, which can be a strong (and inaccurate) assumption. This also requires further adaptation of sediment/obstruction interactions to account for sediment trapping, for instance.

Specifically for upward obstructions such as vegetation, a more radical but pragmatic solution is to replace the OBSTRCUTIONS module with an empirical “obstruction-representative” macro-roughness length in the 3D hydrodynamic model. This option, used in previous studies (Chen et al., 2007; Vargas-Luna et al., 2015), has no additional impact on the computation time step and is less complex to implement. However, it comes with several drawbacks. The vertical discretization must align with the roughness length, meaning the roughness length cannot exceed the first layer's thickness. While this method can reasonably and efficiently simulate average dynamics, the complex vertical velocity profile, and typically the bottom velocity, may not be accurately computed. This becomes problematic when coupled with sediment dynamics or biogeochemical models.

The choice between full 3D, 3D/2D, or roughness length models is ultimately user-dependent, based on the main research question and its minimum requirements for key processes to reproduce.

4.3.2. Upscaling challenge #2: the horizontal description

Regional models typically encompass areas ranging from O(100 km^2) to O(1000 km^2) or larger, with typical mesh size is O(100 m). At this spatial scale, the sub-grid meadows' patchiness can be significant. The primary challenge lies in upscaling the effects of these patches to a larger scale. A straightforward initial solution is to multiply the meadow coverage fraction by the obstruction density. However, this assumes that patches interact independently with the flow, which is not the case when obstruction patches are relatively close to each other (El Allaoui *et al.*, 2016) or when they are sparse (Coulthard *et al.*, 2005).

A second option builds upon the previous solution by incorporating a non-linear transfer function. This would necessitate future or further investigations into the influence of patchiness at the grid cell scale, testing a wide variety of obstruction configurations and densities within a grid cell to establish a reliable transfer function. However, this function would be dependent on the type of obstruction.

A final method to consider involves downscaling the hydrodynamics model to match the resolution of the patchiness, based on the approach developed by Volp et al. (2013). This approach accounted for high-resolution bathymetry and bottom roughness at the subgrid scale. While this option would be tailored to our problem's scale, it would likely be more time-consuming.

5. Conclusions

We have developed the generic OBSTRUCTIONS module designed to represent both upward and downward, rigid or flexible vegetation, and anthropogenic structures such as shellfish farms (long-line farms, oyster table blocks), windfarm piles, or pontoons. Obstructions can take the form of cylinders or parallelepipeds and are described by a limited number of parameters. This module can be integrated with any hydrodynamic coastal model, such as MARS3D in the present study. The obstruction-flow interactions are based on a k-ε turbulent closure model (Temmerman et al., 2005) and can be used in either 3D or 2D mode. Bending is accounted for, and algorithms are available either based on empirical relationships derived from experimental studies (Ganthy et al., 2015) or from an iterative multi-element physical model (Abderhrman, 2007). This module allows for the incorporation of multiple obstructions within a single mesh, which is valuable when modeling ecosystem dynamics.

The generic and reliable nature of this module was demonstrated by implementing four different obstruction types: short and long seagrass meadows, as well as two anthropogenic structures—mussel long-lines and oyster tables. Simulated velocities were compared with reference observations or numerical studies and yielded excellent results with minimal calibration efforts (i.e., only specifying obstruction features and using an average drag coefficient). Specific calibration for the drag coefficient can be considered to further improve model accuracy if necessary.

This module was developed with the aim of simulating integrated coastal ecosystem dynamics, *i.e.*, coupling physical, biogeochemical, and ecological models. Upscaling obstruction interactions from individual systems to regional scales requires careful attention to limit computational costs. Further investigations are needed to account for the spatially heterogeneous extension of obstructions, particularly large patch/block interactions within an O(100x100) m^2 model cell, corresponding to the typical cell size used in coastal models. This coupled model will then provide the opportunity to explore the future trajectories of vulnerable coastal systems in response to global change, or to devise restoration measures for engineered coastal systems.

Nomenclature

3D/2D	Three/Two dimensional
DO	Downward obstruction
FCT	Flux Corrected Transport
MARS	Model for Application at Regional Scale
O3D	Upward obstruction in mid-water
UP	Upward obstruction
A	Horizontal cross-sectional obstruction area per unit area (-)
A_{tot}	Total (over all obstructions variables) horizontal cross-sectional obstruction area per unit area (-)
b	Frontal area of individual obstruction element (m²)
$c_{2\varepsilon}$, c_{μ}	Turbulence coefficients (-)
c_h	Coefficient for exponential decay of obstruction height (-)
c_{lz}	Coefficient for typical size of eddies (-)
c, $c_{z0,abd}$	Coefficient for obstructions roughness height
C_D	Drag coefficient for obstructions (-)
d_0	Diameter of obstruction element, in case of cylinder-like (m)
d_h	Displacement height of velocity profile (m)
dx, dy	Horizontal grid discretization in x and y direction (m)
dz	Vertical grid discretization (m)
f_{xy}	Horizontal fraction of grid cell occupied by obstructions (-)
f_z	Vertical fraction of layer occupied by obstructions (-)
F_u, F_v	Friction force acting on flow in x and y directions ($N.m^{-3}$)
$F_{u,tot}$, $F_{v,tot}$	Total (over all obstructions variables) friction force acting on flow in x and y directions ($N.m^{-3}$)
Fx, Fz	Horizontal (along the flow) and vertical forces acting on an obstruction element ($N.m^{-3}$)
Fxz	Force acting alongside of an obstruction element ($N.m^{-3}$)
g	Gravitational acceleration ($m.s^{-2}$)
h	Effective bent height of obstruction (m)
h_0	Height of unbent obstruction (m)
H	Total water depth
i	Indice of obstruction variable
j	Indice of measured location in velocity profiles
k	Turbulent kinetic energy ($m^2.s^{-2}$)
L	Typical size of eddies (m)
L_{tot}	Total (over all obstructions variables) typical size of eddies (m)
LAI	Leaf Area Index (-)
N	Sample size of model or observation values (-)
n	Number of obstruction elements per unit area (m^{-2})
n_0	Total number of obstruction elements per unit area (m^{-2})
n_{seg}	Number of segment for a single obstruction element (-)
n_{obst}	Number of obstruction variables
NRMSE	Normalized root mean square error (%)
$RMSE$	Root mean square error ($m.s^{-1}$)
s	Indices of the segment of obstruction element
t	Time
t_0	Thickness of an obstruction element in case of parallelepiped-like (m)
t_e	Effective projected thickness (along the flow) of an obstruction element in case of parallelepiped-like (m)
T	Work spent by the fluid ($m^2.s^{-3}$)
U_{mes}	Measured flow velocity ($m.s^{-1}$)

U_{mod}	Simulated flow velocity (m.s^{-1})
U_{∞}	Depth averaged free stream velocity (m.s^{-1})
u,v	Flow velocity in x and y directions (m.s^{-1})
w	Width (across the flow) of an obstruction element in case of parallelepiped-like (m)
x,y	Horizontal position/coordinates (m)
z	Height above the bed (m)
z_0	Bottom roughness length without obstructions (m)

α	Attenuation coefficient for flow within the obstruction canopy
ε	Turbulent energy dissipation (m^2.s^{-3})
$\Delta RMSD$	Normalized difference of root-mean-square deviation (%)
θ	Deflection angle of obstruction from the vertical direction (radian)
κ	van Karman's constant
ν	Molecular viscosity (m^2.s^{-1})
ν_t	Eddy viscosity (m^2.s^{-1})
ρ	Water density (kg.m^{-3})
ρ_{obst}	Obstruction density (kg.m^{-3})
σ_k, σ_{ε}	Turbulent Prandtl-Schmidt coefficients for self-mixing turbulence (-)
τ_{ε}	Energy dissipation timescale (s)

CRediT statement

Florian Ganthy: Conceptualization, Methodology, Software, Data Curation, Writing – Original Draft. **Romaric Verney:** Conceptualization, Methodology, Writing – Review & Editing. **Franck Dumas:** Methodology, Software, Writing – Review & Editing.

Acknowledgments

The authors acknowledge the Pôle de Calcul et de Données Marine (PCDM) for providing DATARMOR facilities (storage, data access and computational ressources). We would also like to thank Solène Le Gac for her careful proof reading as well as the reviewers for their constructive comments which helped us to improve the structure, style, and understanding of our manuscript.

Fundings

This research was supported by IFREMER (the French Institute for Research and Sea Exploitation) and by the French Research National Agency (ANR) in the frame of the Investments for the Future Program, within the Cluster of Excellence COTE (ANR-10-LABX), as part of ZODARSED project.

References

Abdelrhman, M.A., 2003. Effect of eelgrass *Zostera marina* canopies on flow and transport. *Mar. Ecol. Prog. Ser., 248:67-83.*

Abdelrhman, M.A., 2007. Modeling coupling between eelgrass *Zostera marina* and water flow. *Mar. Ecol. Prog. Ser., 338:81-96.*

Auby, I., Oger-Jeanneret, H., Rigouin, L., Trut, G., Cognat, M., Ganthy, F., Gouriou, L., Bujan, S., Gouillieux, B., Dalloyau, S., Feigne, C., Pere, C., Aubert, F., 2018. Suivi stationnel (2006-2017) des herbiers de zostères (Zostera noltei et Zostera marina) et calcul de l'indicateur "Angiospermes" (2017) dans la masse d'eau côtière FRFC06. Arcachon amont – Bassin Hydrographique Adour-Garonne. RTS/ODE/UL/LER/AR/18-010, 56 pp. https://archimer.ifremer.fr/doc/00451/56239/

Beudin, A., Kalra, T.S., Ganju, N.K., Warner, J.C., 2017. Development of a coupled wave-flow-vegetation interaction model. *Computers & Geosciences, 100:76-86.* DOI: 10.1016/j.cageo.2016.12.010

Boothroyd, R.J., Hardy R.J., Warburton, J., Marjoribanks, T.I., 2016. The importance of accurately representing submerged vegetation morphology in the numerical prediction of complex river flow. *Earth Surf. Process. Landforms, 41:567-576.* DOI: 10.1002/esp.3871

Bouma, T.J., van Duren L.A., Temmerman S., Claverie T., Blanco-Garcia, A., Ysebaert, T., Herman, P.M.J., 2007. Spatial flow and sedimentation patterns within patches of epibenthic structures: Combining field, flume and modelling experiments. *Cont. Shelf. Res., 27:1020-1045.* DOI: 10.1016/j.csr.2005.12.019

Carr, J., D'Odorico, P., McGlathery, K., Wiberg, P., 2010. Stability and bistability of seagrass ecosystems in shallow coastal lagoons: Role of feedbacks with sediment resuspension and light attenuation. *J. Geophys. Res., 115:G03011.* DOI: 10.1029/2009JG001103

Casamitjana, X., Pujol, D., Colomer, J., Serra, T., 2012. Application of a k-ε formulation to model the effect of submerged aquatic vegetation on turbulence induced by an oscillating grid. *Cont. Shelf Res., 34:1-6.* DOI: 10.1016/j.csr.2011.11.003

Chen, S.-N., Sanford, L.P., Koch, E.W., Shi, F., North, E.W., 2007. A nearshore model to investigate the effects of seagrass beds geometry on wave attenuation and suspended sediment transport. *Estuar. Coast., 30(2):296-310.*

Coulthard, T.J., 2005. Effects of vegetation on braided stream pattern and dynamics. *Water Ressources Res., 41:W04003.* DOI:10.1029/2004WR003201

Delaux, S., Stevens, C.L., Popinet, S., 2011. High-resolution computational fluid dynamics modelling of suspended shellfish structures. *Environ. Fluid Mech., 11 :405-425.* DOI: 10.1007/s10652-010-9183-y

Dijkstra, J.T., Uittenbogaard, R.E., 2010. Modeling the interaction between flow and highly flexible aquatic vegetation. *Water Resour. Res., 46:W12547.* DOI: 10.1029/2010WR009246

Donatelli, C., Ganju, N.C., Fagherazzi, S., Leonardi, N., 2018. Seagrass impact on sediment exchange between tidal flats and salt marsh, and the sediment budget of shallow bays. *Geophys. Res. Lett., 45:4933-4943.* DOI: 10.1029/2018GL078056

Duarte, P., Alvarez-Salgado, X. A., Fernándeez-Reiriz, M.J., Piedracoba, S., Labarta, U., 2014. A modeling study on the hydrodynamics of coastal embayment occupied by mussel farms (Ria de Ares-Betanzos, NW Iberian Peninsula). *Estuar. Coast. Shelf Sci., 147:42-55.* DOI: 10.1016/j.ecss.2014.05.021

El Allaoui, N., Serra, T., Colomer, J., Soler, M., Casamitjana, X., Oldham C., 2016. Interactions between fragmented seagrass canopies and the local hydrodynamics. *PloS ONE, 11(5):e0156264.* DOI: 10.1371/journal.pone.0156264

Fagherazzi, S., Kiwan, M.L., Mudd, S.M., Guntenspergen, G.R., Temmerman, S., D'Alpaos, A., van de Koppel, J., Rybczyk, J.M., Reyes, E., Craft, C., Clough, J., 2012. Numerical models of salt marsh evolution: ecological, geomorphic and climatic factors. *Rev. Geophys., 50:RG1002.* DOI: 10.10219/2011RG000359

Fonseca, M.S., Fisher, J.S., 1986. A comparison of canopy friction and sediment movement between four species of seagrass with reference to their ecology and restoration. *Mar. Ecol. Prog. Ser., 29 :15-22.*

Ganthy, F., 2011. Rôle des herbiers de zostères (*Zostera noltii*) sur la dynamique sédimentaire du Bassin d'Arcachon. PhD thesis, University of Bordeaux, 284 p. https://archimer.ifremer.fr/doc/00060/17170/

Ganthy, F., Soissons, L., Sauriau, P.G., Verney, R., Sottolichio, A., 2015. Effect of short flexible seagrass *Zostera noltei* on flow, erosion and deposition processes determined using flume experiment. *Sedimentology, 62:997-1023.* DOI: 10.1111/sed.12170

Gao, G., Falconer, R.A., Lin, B., 2011. Modelling open channel flows with vegetation using three-dimensional model. *J. Wat. Res. Prot., 3:114-119.* DOI: 10.4263/jwarp.2011.32013

Gaurier, B., Germain, G., Kervella, Y., Davourie, J., Cayocca, F., Lesueur, P., 2011. Experimental and numerical characterization of an oyster farm impact on the flow. *Eur. J. Mech. B/Fluids, 30:513-525.* DOI: 10.1016/j.eurmechflu.2011.05.001

Giles, H., Pilditch, C.A., Bell, D.G., 2006. Sedimentation from mussel (*Perna canaliculus*) culture in the Firth of Thames, New Zealand: Impacts on sediment oxygen and nutrient fluxes. *Aquaculture, 261:125-140.* DOI: 10.1016/j.aquaculture.2006.06.048

Guillaud, J.F., Andrieux, F., Ménesguen, A., 2000. Biogeochemical modelling in the Bay of Seine (France): an improvement by introducing phosphorus in nutrient cycles. *J. Mar. Sys., 25:369-386.*

Harstein, N.D., Rowden, A.A., 2004. Effect of biodeposits from mussel culture on macroinvertebrate assemblages at sites of different hydrodynamic regime. *Mar. Env. Res., 57:339-357.* DOI: 10.1016/j.marenvres.2003.11.003

Huret, M., Sourisseau, M., Petitgas, P., Struski, C., Léger, F., Lazure, P., 2013. A multi-decadal hindcast of a physical-biogeochemical model and derived oceanographic indices in the Bay of Biscay. *J. Mar. Sys., 109-110:S77-S94.* DOI: 10.1016/j.marsys.2012.02.009

Kaiser, M.J., Laing, I., Utting, S.D., Burnell, G.M., 1998. Environmental impacts of bivalve mariculture. *J. Shellfish Res., 18:347-360.*

Kervella, Y., Germain, G., Gaurier, B., Facq, J.V., Cayocca, F., Lesueur, P., 2010. Experimental study of the near-field impact of an oyster table on the flow. *Eur. J. Mech. B/Fluids, 29:32.42.* DOI: 10.1016/j.euromechflu.2009.09.002

Kombiadou, K., Ganthy, F., Verney, R., Sottolichio, A., 2014. Modelling the effects of Zostera noltei meadows on sediment dynamics: application to the Arcachon lagoon. *Ocean Dyn., 64:1499-1516.* DOI: 10.1007/s10236-014-0754-1

Lacy, J.R., Wyllie-Echeverria, S., 2011. The influence of current speed and vegetation density on flow structure in two macrotidal eelgrass canopies. *Limnol. Oceanogr., 1:38-55.* DOI: 10.1215/21573698-1152489

Lazure, P., Dumas, F., 2008. An external-internal mode coupling for a 3D hydrodynamical model for applications at regional scale (MARS). *Adv. Water Resour., 31:233-250.* DOI: 10.1016/j.adwatres.2007.06.010

Lefebvre A., Thompson, C.E.L., Amos, C.L., 2010. Influence of *Zostera marina* canopies on unidirectional flow, hydraulic roughness and sediment movement. *Cont. Shelf Res., 30:1783-1794.* DOI: 10.1016/j.csr.2010.08.006

Le Hir, P., Monbet, Y., Orvain, F., 2007. Sediment erodability in sediment transport modelling: Can we account for biota effects ? *Cont. Shelf Res., 27:1116-1142.* DOI: 10.1016/j.csr.2005.11.016

Le Hir, P., Cayocca, F., Waeles, B., 2011. Dynamics of sand and mud mixtures: A multi-process-based modelling strategy. *Cont. Shelf Res., 31:S135-S149.* DOI: 10.1016/j.csr.2010.009

McKindsey, C.W., Archambault, P., Callier, M.D., Olivier, F., 2011. Influence of suspended and off-bottom mussel culture on the sea bottom and benthic habitats: a review. *Can. J. Zool., 89:622-646.* DOI: 10.1139/Z11-037

Mengual, B., Le Hir, P., Cayocca, F., Garlan, T., 2017. Modelling fine sediment dynamics: Toward a common erosion law for fine sand, mud and mixtures. *Water, 9:564.* DOI: 10.3390/w9080564

Montefalcone, M., 2009. Ecosystem health assessment using the Mediterranean seagrass *Posidonia oceanica*: a review. *Ecol. Indic., 9:595-604.* DOI: 10.1016/j.ecolind.2008.09.013

Morin, J., Leclerc, M., Secretan, Y., Boudreau, P., 2000. Integrated two-dimensional macrophytes-hydrodynamic modeling. *J. Hydraul. Res., 38 :163-172.* DOI: 10.1080/00221680009498334

Nepf, H.M., 1999. Drag, turbulence, and diffusion in flow through emergent vegetation. *Water Resour. Res., 35(2):479-489.*

Nepf, H.M., Vivoni, E.R., 2000. Flow structure in depth-limited, vegetated flow. *J. Geophys. Res. 105(C12) :28,547-28,557.*

Plew, D.R., 2010. Depth-averaged drag coefficient for modeling flow through suspended canopies. *J. Hydraul. Eng., 137(2)*. DOI: 10.1061/(ASCE)HY.1943-7900.0000300

Plew, D.R., Stevens, C.L., Spigel, R.H., Harstein, N.D., 2005. Hydrodynamic implication of large offshore mussel farms. *IEEE J. Ocean. Engin., 30(1):95-108*. DOI: 10.1109/JOE.2004.841387

Plus, M., Chapelle, A., Deslous-Paoli, J.M., Auby, I., 2003. Modelling seasonal dynamics of biomasses and nitrogen contents in a seagrass meadow (*Zostera noltii* Hornem.): application to the Thau lagoon (French Mediterranean coast). *Ecol. Model., 161(3):211-236.* DOI: 10.1016/S0304-3770(03)00089-5

Soissons, L.M., van Katwijk, M.M., Peralta, G., Brun, F.G., Cardosso, P.G., Grilo T.F., Ondiviela, B., Recio, M., Valle, M., Garmendia, J.M., Ganthy, F., Auby, I., Rigouin, L., Godet, L., Fournier, J., Desroy, N., Barillé, L., Kadel, P., Asmus, R., Herman, P.M.J., Bouma, T.J., 2017. Seasonal and latitudinal variation in seagrass mechanical traits across Europe : The influence of local nutrient status and morphometric plasticity. *Limnol. Oceanogr. 63(1) :37-46.* DOI: 10.1002/lno.10611

Sornin, J.-M., 1981. Influence des installations conchylicoles sur l'hydrologie et sur la morphologie des fonds. *Rev. Trav. Inst. Pêches. Marit., 45(2):127-139.* https://archimer.ifremer.fr/doc/00000/1900/

Temmerman, S., Bouma, T.J., Govers, G., Wang, Z.B., De Vries M.B., Herman, P.M.J., 2005. Impact of vegetation on flow routing and sedimentation patterns: Three-dimensional modeling for a tidal marsh. *J. Geophys. Res., 110:F040119.* DOI: 10.1029/2005JF000301

Uittenbogaard, R.E., 2003. Modelling turbulence in vegetated aquatic flows. *Proceedings of International Workshop on Riparian Forest Vegetated Channels: Hydraulic, Morphological and Ecological Aspects, RIPFOR, Trento, Italy.*

Umlauf, L., & Burchard, H., 2003. A generic length-scale equation for geophysical turbulence models. *Journal of Marine Research*, *61*(2), 235-265.

Vargas-Luna, A., Crosato, A., Calvani, G., Uijttewaal, W.S.J., 2016. Representing plants as rigid cylinders in experiments and models. *Adv. Water Resour., 93:205-222.* DOI: 10.1016/j.advwatres.2015.10.004

Ward, L.G., Kemp, W.M., Boynton, W.R., 1984. The influence of waves and seagrass communities on suspended particulates in an estuarine embayment. *Mar. Geol., 59:85-103.*

Weise, A.M., Cromey, C.J., Callier, M.D., Archambault, P., Chamberlain, J., McKindsey, C.W., 2009. Shelfish-DEPOMOD: Modelling the biodeposition from suspended shellfish aquaculture and assessing benthic effects. *Aquaculture, 288:239-253.* DOI: 10.1016/j.aquaculture.2008.12.001

Weitzman, J.S., Zeller, R.B., Thomas, F.I.M., Koseff, J.R., 2015. The attenuation of current- and wave-driven flow within submerged multispecific vegetative canopies. *Limnol. Oceanogr., 60:1855-1874.* DOI: 10.1002/lno.10121

Zhang, M., Li, C.W., Shen, Y., 2013. Depth-averaged modeling of free surface flows in open channels with emerged and submerged vegetation. *Appl. Mathem. Mod., 37:540-553.* DOI: 10.1016/j.apm.2012.02.049

Appendix A: Description of the Abdelrhman's (2003) method for theoretical velocity profile computation

The flow velocity above the obstruction canopy at a distance *z* above the bed ($u_{above}(z)$) is expressed as:

$$u_{above}(z) = \frac{u^{*}_{can}}{\kappa} \cdot \log\left(\frac{z - d_h + z_0}{Z_0}\right) \tag{A1}$$

where u^{*}_{can} is the friction velocity for the canopy, κ is von Karman's constant (0.4), d_h is the displacement height of velocity profile above the canopy and Z_0 is the roughness height for obstruction canopy.

The displacement height of velocity profile (d_h) and the roughness height for obstruction canopy (Z_0) are then expressed as:

$$d_h = \frac{c_{z0,abd} \cdot h^2 \cdot w}{(a + c_{z0,abd} \cdot h \cdot w)} \tag{A2}$$

$$Z_0 = \frac{0.5 \cdot w \cdot h^2 \cdot a}{(a + c_{z0,abd} \cdot h \cdot w)^2} \tag{A3}$$

Where $c_{z0,abd}$ is a calibration coefficient and a is the horizontal area per obstruction element ($a = \pi \cdot \frac{w}{2} \cdot \frac{t_e}{2} \cdot \frac{h}{h_0}$ for cylinder-like obstructions and $a = w \cdot t_e \cdot \frac{h}{h_0}$ for parallelepiped-like obstructions).

The flow velocity within the obstruction canopy at a distance *z* above the bed ($u_{can}(z)$) is expressed as:

$$u_{can}(z) = u_h \cdot \exp\left[\alpha \cdot \left(\frac{z}{h} - 1\right)\right] \tag{A4}$$

Where u_h is the flow velocity at the top of the canopy ($z=h$) and α is an attenuation coefficient given by:

$$\alpha = h \cdot \left(\frac{C_D \cdot b}{2 \cdot \lambda^2} \right)^{1/3} \quad \text{(A5)}$$

Where b is the frontal area of the individual obstruction element ($b = w \cdot h$) and λ is the mixing length of the turbulent flow within the obstruction, assumed to be equal to d_h.

Finally, u^*_{can} is calculated from the conservation of fluid mass between the water column without and with obstruction:

$$\int_0^H \frac{u^*}{\kappa} \cdot \log\left(\frac{z+z_0}{z_0} \right) \cdot dz = \int_0^h u_h \cdot \exp\left[\alpha \cdot \left(\frac{z}{h} \right) - 1 \right] \cdot dz + \int_h^H \frac{u^*_{can}}{\kappa} \cdot \log\left(\frac{z-d_h+z_0}{Z_0} \right) \cdot dz \quad \text{(A6)}$$

So that:

$$u^*_{can} = \frac{u^* \left[(H+z_0) \cdot \log\left(\frac{H+z_0}{z_0} \right) - H \right]}{\frac{h}{\alpha} \cdot \log\left(\frac{h-d_h+z_0}{Z_0} \right) \left(1-e^{\alpha} \right) + \left(H-d_h+z_0 \right) \cdot \log\left(\frac{H-d_h+z_0}{Z_0} \right) - \left(h-d_h+z_0 \right) \cdot \log\left(\frac{h-d_h+z_0}{Z_0} \right) + \left(H-h \right)}$$

(A7)

Where H is the total water depth, and u^* is friction velocity for bed without obstructions.

Appendix B: Description of the Abdelrhman's (2007) method for the computation of bent obstruction height

The algorithm to compute bending angle for flexible obstructions is based on the balance between drag, lift, friction, weight, and buoyancy forces on a single obstruction element, subdivided into a user-defined number of segment (n_{seg}). Each segment of obstruction element also has a length (l_{seg}):

$$l_{seg} = h_0 / n_{seg} \tag{B1}$$

The net vertical force is computed as the difference between weight and buoyancy:

$$F_{vertical} = \left(\rho - \rho_{obst}\right) \cdot g \cdot w \cdot t_0 \cdot l_{seg} \tag{B2}$$

where ρ is water density, ρ_{obst} is obstruction's bulk density, and g is the gravitational acceleration.

When flow passes around obstruction element it generates form drag in the direction of motion. The form drag can be expressed by:

$$F_{drag} = 0.5 \cdot \rho \cdot C_D \cdot uv(z)^2 \cdot w \cdot l_{seg} \cdot \cos(\theta) \tag{B4}$$

where $uv(z)$ is the free stream velocity at height z above the bed, and θ is the deflection angle of a segment from the horizontal. The angle θ remains unknown in this part of the analysis. Roughness on obstruction element's surface generates the skin friction drag force, which aligns in the direction of the element and can be expressed as:

$$F_{skin} = 0.5 \cdot \rho \cdot C_f \cdot \left(uv(z) \cdot \sin(\theta)\right)^2 \cdot 2 \cdot w \cdot l_{seg} \tag{B5}$$

where C_f is the skin friction coefficient assumed to the same for the two sides of an obstruction element. The skin friction is computed from the Reynolds number (R):

$$C_{lift} = 0.074 \cdot R^{-1/5} \tag{B6}$$

$$R = \frac{uv(z) \cdot w \cdot \rho}{\mu} \tag{B7}$$

where μ is the dynamic viscosity.

Finally, a lift force (vertical) is produced when the flow passes around element:

$$F_{lift} = 0.5 \cdot \rho \cdot C_{lift} \cdot uv(z)^2 \cdot w \cdot l_{seg} \cdot \sin(\theta) \tag{B8}$$

where C_{lift} is the lift coefficient (0.1). For θ ranging between 0 and π/2 the lift force will be downward, on the contrary, for angle ranging between π/2 and π the lift force will be upward.

Then, the algorithm solves the balance of forces for each segment using a downward procedure. When the bending angle of a segment changes, its vertical location above the bottom will change accordingly, hence it will experience different local velocities. Both the bending angle of the segment (θ_s) and the local velocity uv_s at the s^{th} element are taken into account.

At the highest segment (s=1), the segment is deflected by the resultant of drag, lift, skin, weight and buoyancy forces, which produces tensile force in the segment. All forces are then decomposed into horizontal (x) and vertical (z) components to calculate the magnitude and direction of the resultant force. All moments are summed at the lower segment joint and equated to zero, allowing to calculate the bending angle of the segment:

$$\begin{aligned} &0.5 \cdot C_D \cdot \rho \cdot uv_{s=1}^2 \cdot w \cdot l_{seg} \cdot \frac{l_{seg}}{2} \cdot \cos\left(\theta_{s=1}\right)^2 + 0.5 \cdot C_{lift} \cdot \rho \cdot uv_{s=1}^2 \cdot w \cdot l_{seg} \cdot \frac{l_{seg}}{2} \cdot \sin\left(\theta_{s=1}\right)^2 \\ &-\left(\rho - \rho_{obst}\right) \cdot g \cdot w \cdot t_e \cdot l_{seg} \cdot \frac{l_{seg}}{2} \cdot \sin(\theta_{s=1}) = 0 \end{aligned} \tag{B9}$$

In eq. (B8), the only unknown is $\theta_{s=1}$ which is obtained iteratively. As the top-most segment only has a lower joint, so reaction $Fxz_{s=1}$ should fall in the direction of that segment. This implies for the segment to be stable that the summation of all components of force in the x and z directions should be equal to zero:

$$Fx_{s=1} + 0.5 \cdot C_D \cdot \rho \cdot uv_{s=1}^2 \cdot w \cdot l_{seg} \cdot \cos(\theta_{s=1}) + 0.5 \cdot C_f \cdot \rho \cdot uv_{s=1}^2 \cdot w \cdot l_{seg} \cdot \sin(\theta_{s=1})^3 = 0 \tag{B10}$$

$$\begin{aligned} &Fz_{s=1} - 0.5 \cdot C_{lift} \cdot \rho \cdot uv_{s=1}^2 \cdot w \cdot l_{seg} \cdot \sin(\theta_{s=1}) + (\rho - \rho_{obst}) \cdot w \cdot l_{seg} \cdot t_e \\ &+ 0.5 \cdot C_f \cdot \rho \cdot uv_{s=1}^2 \cdot w \cdot l_{seg} \cdot \sin(\theta_{s=1})^2 \cdot \cos(\theta_{s=1}) = 0 \end{aligned} \tag{B11}$$

where $Fx_{s=1}$ and $Fz_{s=1}$ are the horizontal and vertical components, respectively, of the reaction at the lower joint. The reaction $Fxz_{s=1}$ alongside of a segment ($Fxz_{s=1} = \left(Fx_{s=1}^2 + Fz_{s=1}^2\right)^{1/2}$) is obtained by substituting the value of $\theta_{s=1}$ in (B9) and (B10). A force of equal magnitude but opposite direction to this reaction then transfers the effects of all forces on the top-most segment (s=1) to the next one (s=2). The same procedure is then applied to all segments. For an intermediate segment s, equations (B8), (B9) and (B10) become:

$$\begin{aligned} &0.5 \cdot C_D \cdot \rho \cdot uv_s^2 \cdot w \cdot l_{seg} \cdot \frac{l_{seg}}{2} \cdot \cos(\theta_s)^2 + 0.5 \cdot C_{lift} \cdot \rho \cdot uv_s^2 \cdot w \cdot l_{seg} \cdot \frac{l_{seg}}{2} \cdot \sin(\theta_s)^2 \\ &- (\rho - \rho_{obst}) \cdot g \cdot w \cdot t_e \cdot l_{seg} \cdot \frac{l_{seg}}{2} \cdot \sin(\theta_s) + Fx_{s-1} \cdot l_{seg} \cdot \cos(\theta_s) - Fz_{s-1} \cdot l_{seg} \cdot \sin(\theta_s) = 0 \end{aligned} \tag{B12}$$

$$Fx_s + 0.5 \cdot C_D \cdot \rho \cdot uv_s^2 \cdot w \cdot l_{seg} \cdot \cos(\theta_s) + 0.5 \cdot C_f \cdot \rho \cdot uv_s^2 \cdot w \cdot l_{seg} \cdot \sin(\theta_s)^3 + Fx_{s-1} = 0 \tag{B13}$$

$$\begin{aligned} &Fz_s - 0.5 \cdot C_{lift} \cdot \rho \cdot uv_s^2 \cdot w \cdot l_{seg} \cdot \sin(\theta_s) + (\rho - \rho_{obst}) \cdot w \cdot l_{seg} \cdot t_e \\ &+ 0.5 \cdot C_f \cdot \rho \cdot uv_s^2 \cdot w \cdot l_{seg} \cdot \sin(\theta_s)^2 \cdot \cos(\theta_s) + Fz_{s-1} = 0 \end{aligned} \tag{B14}$$

where Fx_s and Fz_s are the horizontal and vertical components of the reaction at the lower joint s respectively. Equation (B11) is first solved iteratively to obtain the value of θ_s which is then substituted in (B12) and (B13) to obtain the reaction force that will act to the next segment.

1206 **Appendix C: Velocity comparison between 3D and 2D formulations for the OYcase**

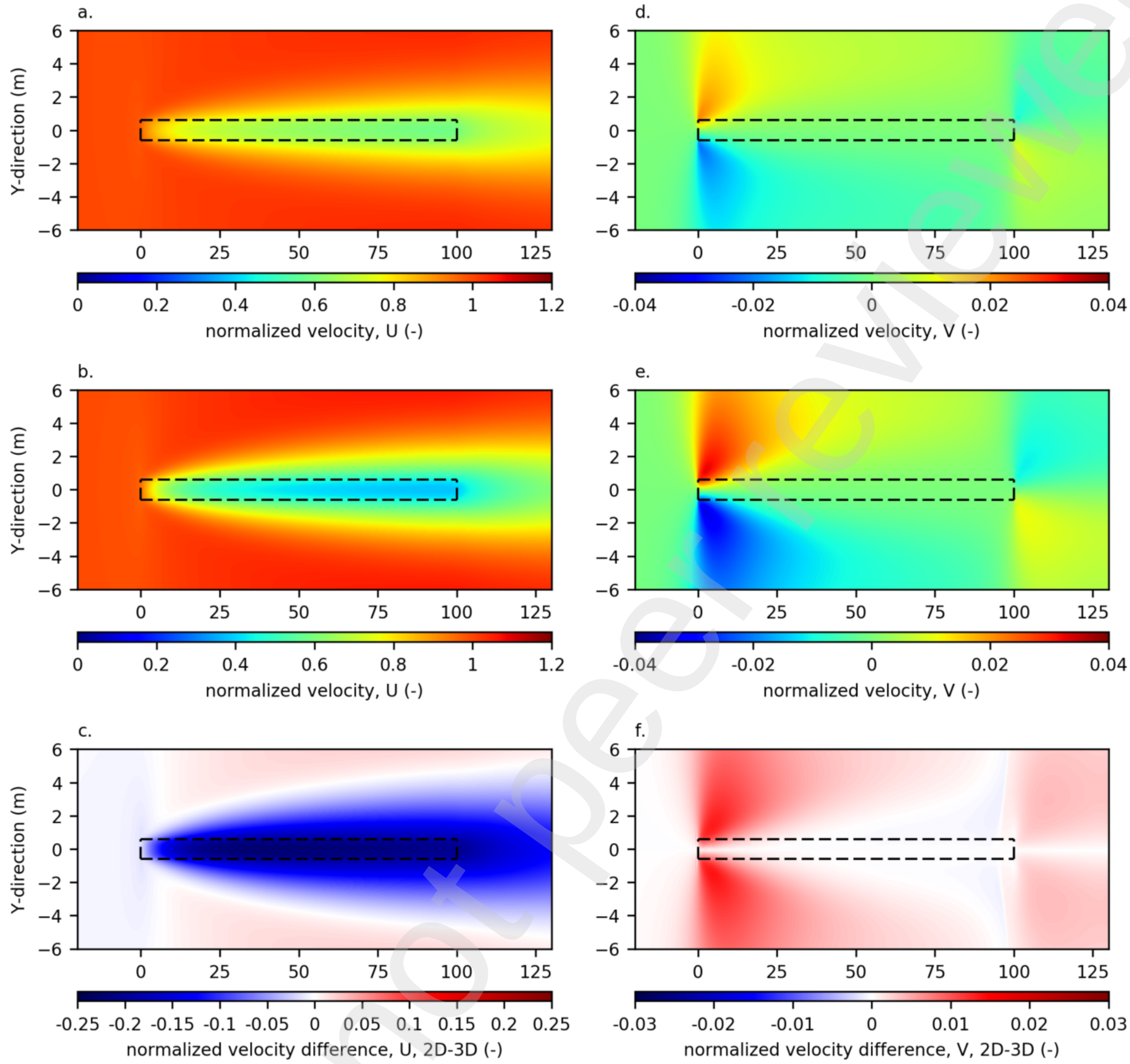

1207

1208 *Figure C1: Depth-averaged normalized velocities simulated for the OYcase using 3D (a. and*
1209 *d.) and 2D (b. and e.), as well as the velocity differences between 3D and 2D formulations (c.*
1210 *and f.), for the longitudinal velocity component (U, left panel, a., b. and c.) and for the lateral*
1211 *velocity component (V, right panel, d., e. and f.). Table locations (bags and tables legs) are*
1212 *indicated by black dotted lines.*

1213